Miner Petrol (2016) 110:223–245
DOI 10.1007/s00710-015-0402-6

ORIGINAL PAPER

# Mineralogy of the P-12 K-Ti-richterite diopside olivine lamproite from Wajrakarur, Andhra Pradesh, India: implications for subduction-related magmatism in eastern India

**Gurmeet Kaur**[1] · **Roger H. Mitchell**[2]

Received: 19 August 2014 / Accepted: 26 July 2015 / Published online: 8 August 2015


**Abstract** The P-12 "para-kimberlite" from Wajrakarur consists of forsteritic olivine, Al-Na-poor diopside, Fe-Ti-rich, Al-poor phlogopite, K-Ti-richterite, spinel, perovskite, cymrite, apatite, barite, Ba-Sr- bearing calcite, gittinsite, witherite, strontianite, and hydrogrossular (hydrogarnet). The rock also contains small clasts consisting dominantly of calcite, with lesser Ba-Sr-bearing calcite, cymrite, barite, strontianite, witherite, apatite, and hydrogrossular. Two generations of forsteritic olivine ($Fo_{80–93}$) crystals are present: common phenocryst-to-microphenocrystal; and rare anhedral macrocrystic olivines. Phlogopite occurs as microphenocrysts and as groundmass poikilitic plates with inclusions of spinel, perovskite, apatite, and chlorite pseudomorphs (after pyroxene). Phlogopites also occur as reaction rims around olivine crystals. The phlogopites have extremely low $Al_2O_3$ (2.2–3.8 wt.%), moderate-to-high FeO (6.9–16 wt.%), $TiO_2$(1.9–4.6 wt.%), and $Na_2O$ (0.4–2.7 wt.%) contents and are enriched in fluorine (up to 6.0 wt.%) and considered to be tetraferriphlogopite. The pyroxenes occur in five parageneses as: (1) phenocrysts and microphenocrysts; (2) small slender crystals(<30 μm) forming part of the groundmass; (3) the cores of richterite crystals; (4) reaction products replacing earlier-formed olivine; (5) acicular crystals mantling carbonate clasts. These pyroxenes do not differ significantly in composition and are all diopsides with minor variation in their $TiO_2$, $Al_2O_3$, $Na_2O$ contents. Titanian-potassium richterite commonly occurs as: (1) groundmass poikilitic plates; (2) small prismatic crystals (<30 μm); (3) reaction rims on olivine and pyroxene crystals. Groundmass poikilitic richterites commonly enclose pyroxene and apatite. Perovskites have a bimodal size distribution. Small (<20 μm) euhedral perovskites are scattered throughout the groundmass, whereas larger (100–300 μm) subhedral-to-euhedral perovskites are patchily-zoned and commonly broken. Micro-clasts consisting of accumulations of perovskite with phlogopite and apatite are also present. Spinels occur as large atoll crystals and small (<20 μm), euhedral-to-subhedral crystals, scattered throughout the groundmass. Some small spinel crystals are also present in the rims of olivine and pyroxene crystals. Atoll spinels are up to 100 μm in size, commonly with single and double cores. Atoll spinels are typically associated with perovskites. The euhedral-to-subhedral small spinels are ulvospinels. The atoll spinels have cores of titanian aluminous magnesiochromite with rims of magnesian titaniferous magnetite. The spinels have compositions which evolve along the lamproite-spinel compositional trend. Zoned calcite crystals occur as residual phases. Late stage residual calcite and carbonate clasts host prismatic cymrite crystals which are interpreted as pseudomorphs after potassium feldspar and/or barite. Subhedral-to-euhedral gittinsite and its Sr-analog are reported for the first time from the groundmass carbonate-chlorite mesostasis of a lamproite. Square-to-rectangular crystals of cymrite and hydrogrossular occur in the carbonate clasts and groundmass material. Barite anhedra commonly occur in the carbonate clasts together with witherite,

Editorial handling: L. G. Gwalani

✉ Roger H. Mitchell
rmitchel@lakeheadu.ca

Gurmeet Kaur
gurmeet28374@yahoo.co.in

[1] Department of Geology, Panjab University, Chandigarh, UT 160014, India

[2] Department of Geology, Lakehead University, Thunder Bay, Ontario, Canada P7B 5E1

strontianite, and Ba-Sr-bearing calcite. The texture and compositions of olivine, phlogopite, spinel, and K-Ti-richterite, together with the presence of cymrite pseudomorphs, possibly after potassium feldspar, demonstrate that this intrusion is a *bona fide* olivine lamproite and not a kimberlite. It is postulated that this, and other lamproites, located adjacent to the Eastern Ghats Mobile Belt, are derived by extensional decompressional melting of ancient subduction zones underlying the cratonic regions.

## Introduction

Diamonds are synonymous with the Indian subcontinent and historical accounts of travellers visiting India in the quest for diamonds are well-documented in the literature (Fareeduddin and Mitchell 2012). The last decades have witnessed a remarkable influx of multi-national mining companies to India, such as Rio Tinto and De Beers, in search, of the diamonds and their primary host rocks. Although kimberlites and lamproites are both diamond-bearing rocks, they are mineralogically and genetically different (Mitchell 1995, 2006). The 10th International Kimberlite Conference (IKC), 2012 held in Bangalore, brought to India many international geoscientists working in the field of diamonds and diamond-hosting rocks. The present work on hypabyssal intrusions in the Wajrakarur region is a result of collaborative work, initiated during the 10th IKC, to investigate the kimberlite and lamproite rocks of India, with special emphasis on their mineralogical-genetic classification. Rocks described as kimberlites and/or lamproites have been reported from the Dharwar, Bundelkhand, and Bastar Cratons of India (Fareeduddin and Mitchell 2012).

The Wajrakarur region is located in the Dharwar Craton and is subdivided into the Eastern and Western Dharwar Cratons. The kimberlites and lamproites so far discovered in the Dharwar Craton occur only in the Eastern Dharwar Craton (Inset of Fig. 1; Neelkantam 2001; Fareeduddin and Mitchell 2012). Recent detailed mineralogical studies of the P2-West, P-5, P-13 intrusions of the Wajrakarur-Lattavaram cluster clearly indicate their affinity with lamproite rather than archetypal kimberlite (Mitchell 2010; Fareeduddin and Mitchell 2012; Gurmeet Kaur et al. 2012a, b, 2013; Gurmeet Kaur and Mitchell 2013). This study of the P-12 intrusion from the Wajrakarur Kimberlite cluster demonstrates the presence of minerals which are typomorphic of lamproites rather than kimberlite i.e.,: titanian-potassium richterite and titanian-potassium-magnesiokatophorite; Al-Na-poor diopside; tetraferriphlogopite; qandilite-poor spinels; and Zr-silicates. Accordingly, we re-classify the P-12 "para-kimberlite" as a *bona fide* olivine lamproite in contrast to the conclusions of previous studies (Rao et al. 2001; Neelkantam 2001; Ravi et al. 2009; Fareeduddin and Mitchell 2012).

## Geological setting

To date, four "kimberlite" fields and three "lamproite" fields have been identified in the Eastern Dharwar Craton (Inset of Fig. 1): (1) Wajrakarur Kimberlite Field; (2) Narayanpet Kimberlite Field; (3) Raichur Kimberlite Field; (4) Tungabhadra Kimberlite Field; (5): Krishna Lamproite Field; (6) Nallamalai Lamproite Field; (7) Ramadugu Lamproite Field (inset of Fig. 1; Reddy 1987; Nayak and Kudari 1999; Ravi *et al*. 1999; Neelkantam 2001; Chalapathi Rao et al. 2004, 2013; Paul *et al*. 2006; Fareeduddin and Mitchell 2012; Gurmeet Kaur and Mitchell 2013). All the of kimberlite and lamproite fields occur as clusters of small hypabyssal intrusions locally referred to as "pipes", regardless of their morphology. For a summary of the geological setting of the kimberlite and lamproite fields of the Dharwar Craton see Fareeduddin and Mitchell (2012).

## Wajrakarur Kimberlite Field

The 31 occurrences of kimberlite-like rocks of the Wajrakarur Kimberlite Field occur as five clusters :(1) Wajrakarur (pipes P-1, P-2, P-6, P-10, P-11, P-12, P-15); (2) Lattavaram (pipes P-3, P-4, P-5, P-7, P-8, P-9, P-13); (3) Chigicherla (pipes CC-1 to CC-5); (4) Kalyandurg (pipes KL-1 to KL-6); (5) Timmasamudram (pipes TK-1 to TK-6). The location and mode of occurrence of each intrusion has been documented in detail by Neelkantam (2001) and Fareeduddin and Mitchell (2012).

Recently, Mitchell (2010), Fareeduddin and Mitchell (2012), Gurmeet Kaur et al. (2012a, b, 2013) and Gurmeet Kaur and Mitchell (2013) reclassified the P-5, P-13, P-3, P-4 and P2-West "kimberlites" as lamproites on the basis of their mineralogy.

## Geology of pipe P-12

The P-12 "parakimberlite", also known as the Chintalmapalle kimberlite, is located approximately 0.75 km north of the village of Chintalmapalle and approximately 10 km east of Wajrakarur (Fig. 1) (Rao et al. 2001; Fareeduddin and Mitchell 2012). The intrusion (130×50 m) trends NE-SW and is emplaced into granitoid country rocks. The morphology of the intrusion at depth is unknown. Diatreme and pyroclastic rocks are not present. The exposure consists of competent steel-grey boulders surrounded by weathered, carbonated, yellowish-green material. The fresh hard kimberlite is exposed only in the south eastern part of the intrusion and is characterized by the presence of olivine, small angular carbonate clasts, and numerous locally-derived crustal xenoliths of granite gneiss, dolerite, amphibolites, and gabbro (Ravi et al.

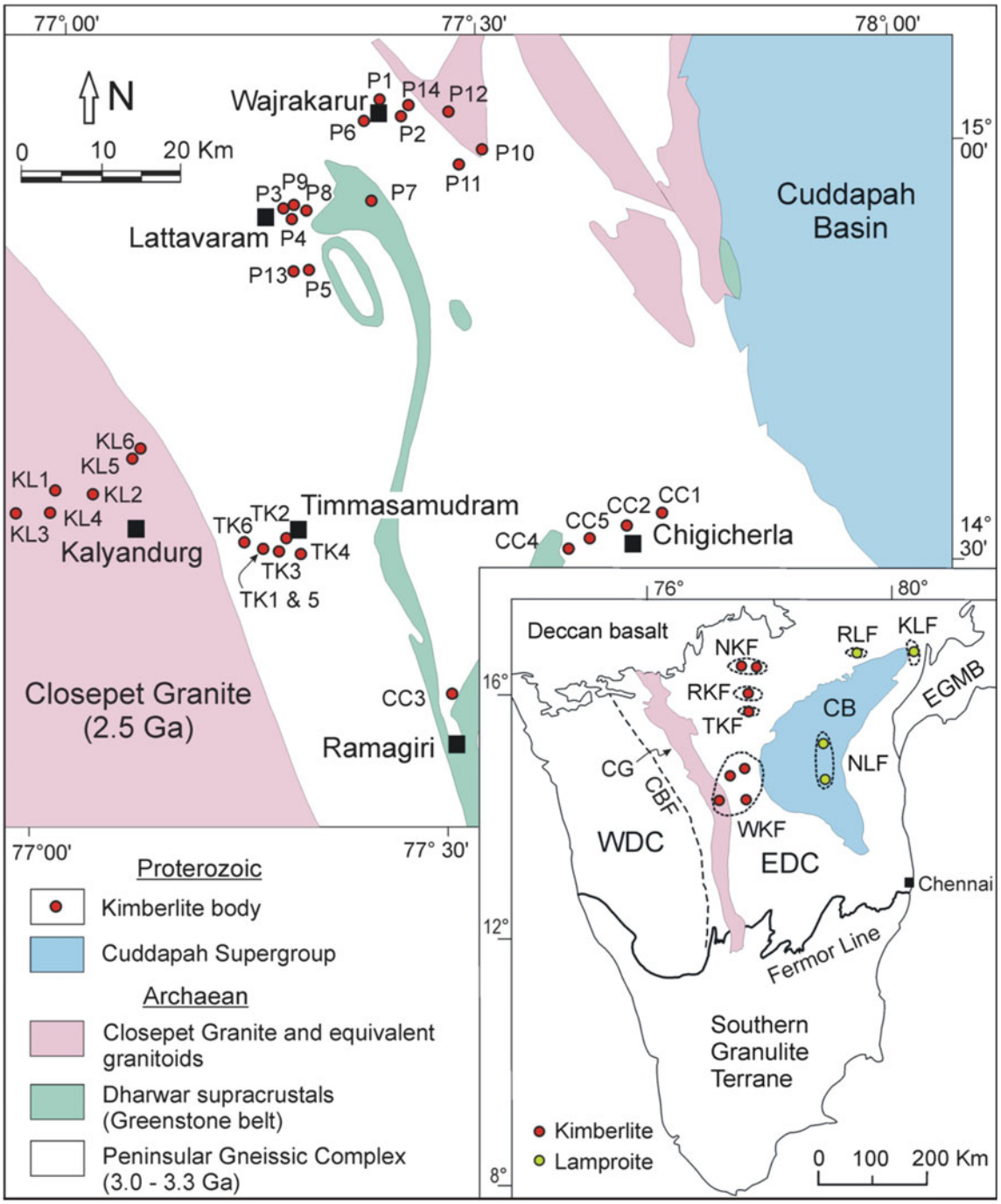


**Fig. 1** Wajrakarur Kimberlite Field consisting of the Wajrakarur, Lattavaram, Kalyandurg, Timmasamudram and Chigicherla clusters, Anantapur district, Andhra Pradesh, India. The location of pipe P-12, and other pipes, in the Wajrakarur cluster are marked on the map. Also shown in the inset map are the locations of the kimberlite and lamproite fields in the Eastern Dharwar Craton. *WKF* Wajrakarur kimberlite field, *NKF* Narayanpet kimberlite field, *RKF* Raichur kimberlite field, *TKF* Tungabhadra kimberlite field, *KLF* Krishna lamproite field, *RLF* Ramadugu lamproite field, *NLF* Nallamalai field

2009; Fareeduddin and Mitchell 2012). Xenoliths and xenocrysts present are: enstatite-garnet pyroxenite; chromian-spinel-garnet pyroxenite; chrome-diopside; ilmenite; spinel; red and orange garnet (Rao et al. 2001; Fareeduddin and Mitchell 2012; Patel et al. 2013). Olivine, phlogopite, perovskite, serpentine, spinel, carbonate, and apatite are the only minerals reported from P-12 by Chalapathi Rao et al. (2013). Processing of the weathered kimberlite sample did not yield any diamonds (Rao et al. 2001; Ravi et al. 2013). Earlier studies did not recognize the presence of the abundant pyroxene and amphibole which we have found to characterize P-12.

## Analytical techniques

Representative samples of P-12 were investigated by back-scattered electron (BSE) imagery and *quantitative* energy dispersive X-ray spectrometry using a Hitachi SU-70 scanning electron microscope at Lakehead University. All raw X-ray data were obtained using a beam current of 300 pA, an accelerating voltage of 20 kV, and 30–60 s counting times, and processed using Oxford Aztec software. Analytical standards used are those given by Liferovich and Mitchell (2005).

## Petrography of P-12

Megascopically, P-12 is greenish-grey in colour with carbonate clasts. Microscopically, the rock exhibits an inequigranular texture consisting of euhedral-to-subhedral, resorbed, rounded-to-anhedral, fractured phenocrysts and microphenocrysts of olivine and pyroxene set in a fine-grained ground mass consisting of pyroxene, phlogopite, richterite, spinel, perovskite, apatite, calcite, barite, chlorite, and serpentine together with accessory cymrite, gittinsite, witherite, and strontianite (Fig. 2a, b, c, d). The rock contains carbonate clasts with opaque-to-brown prisms of pyroxene, cymrite, and hydrogarnet lining the margins of the clasts (Fig. 2b, d). Groundmass tetraferriphologopites are identified by their characteristic deep orange-red colour and reverse pleochroism (Fig. 2c). Oxide phases in the groundmass, perovskite and spinel, are euhedral-to-subhedral, opaque/ brown-black in colour (Fig. 2d).

## Mineral compositions

### Olivine

Olivine occurs as two texturally-distinct varieties, rare macrocrysts and common phenocrysts, and microphenocrysts (Fig. 2a). The macrocrysts are principally anhedral-to-rounded and are partially-to-completely altered to chlorite and serpentine (Fig. 2a). On the basis of their morphology, many macrocrysts appear to be resorbed phenocrysts rather than xenocrysts. The phenocrysts and microphenocrysts are euhedral-to-anhedral in habit (Fig. 3a, b, c, d), with thin alteration rims of chlorite (Fig. 3a, b, c, d).

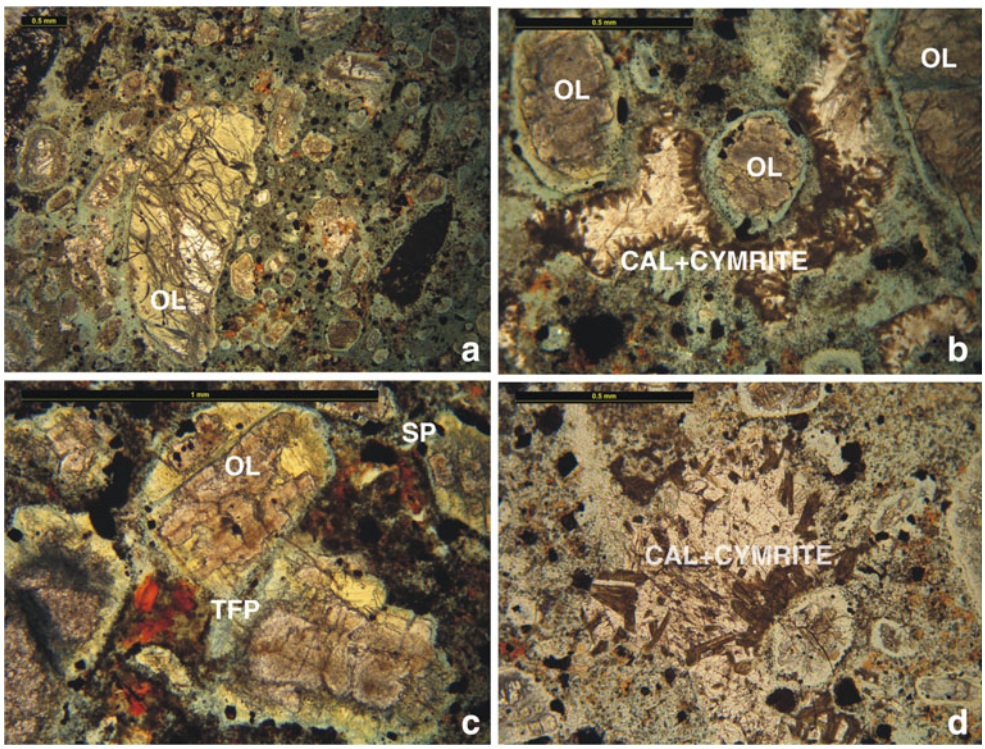


**Fig. 2** **a** The texture of P-12 olivine lamproite illustrating the presence of a resorbed olivine (OL) macrocryst and olivine microphenocrysts set in a fine grained optically non-resolvable groundmass material. The olivine is altered along the rims and fractures to serpentine and chlorite. Plane polarized light (PPL). **b** Ovoid-to-resorbed crystals of olivine (OL) and the irregularly shaped carbonate clasts with prismatic *dark brown* cymrite (CAL+CYMRITE) and pyroxene lining the contact of lamproitic material and carbonate clasts. (PPL). **c** Deep *orange red* tetraferriphlogopite (TFP) occurring as small plates in the groundmass. Also seen are opaque euhedral-to-suhhedral spinels (SP) and perovskites in the groundmass. (PPL). **d** Prismatic brownish crystals of cymrite and pyroxene forming part of a carbonate clast and groundmass material. Also seen are orange-red tetraferriphlogopite and euhedral-to-subhedral opaque spinels and perovskite. (PPL)

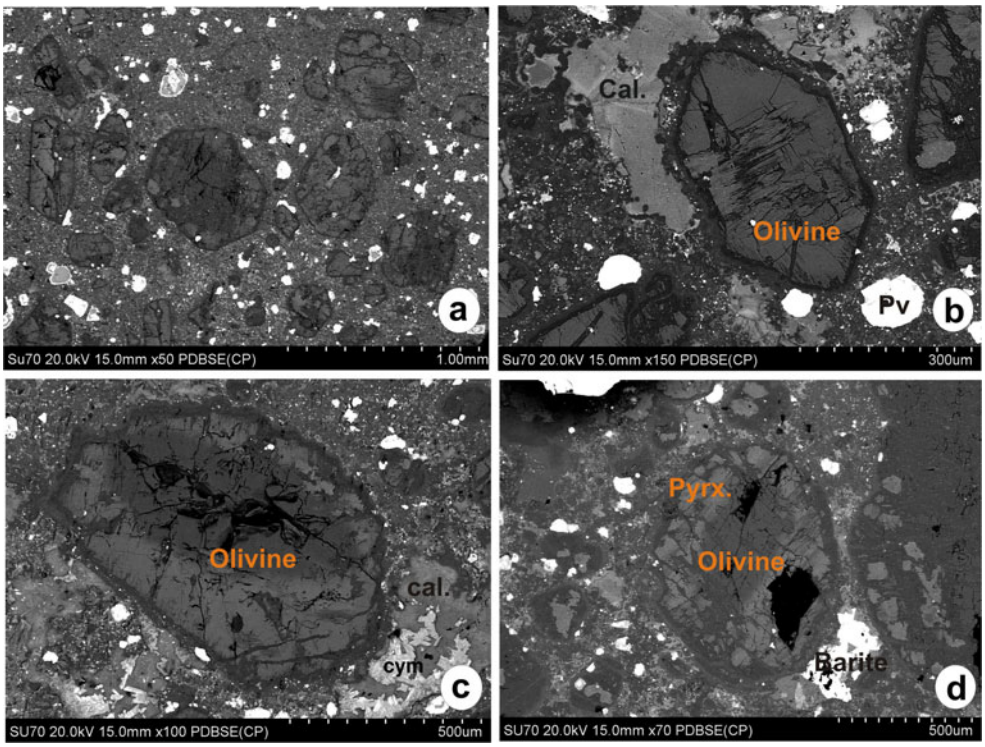


**Fig. 3** **a** Euhedral-to-subhedral olivine microphenocrysts in groundmass material. (BSE image). **b** Euhedral olivine phenocryst partially surrounded by calcite in groundmass material consisting of perovskite, spinel (BSE image). **c** A partially-resorbed zoned olivine in groundmass material. Also seen are cymrite (cym) in the carbonate (cal) material present on the lower right and left side of the olivine crystal (BSE image). **d** An ovoid olivine which has partially-altered to pyroxene (Pyrx) along the rim. Also seen are barite anhedra in the groundmass. (BSE image)

Representative compositions of olivine phenocrysts and microphenocrysts are given in Table 1, and range in composition from $Fo_{92–80.}$ Olivine phenocrysts contain inclusions of perovskite, spinel, apatite, and Ni-sulphide. Phenocrysts and microphenocrysts exhibit reverse and normal zoning (Table 1). Many olivine phenocrysts and microphenocrysts have been altered to chlorite, serpentine, diopside, hydrogarnet, and carbonates along fractures, in their cores and near the rims (Figs. 2b, c, d and 3b, c). Some of the phlogopite is clustered around the outer margins of olivines (Fig. 5d).

## Pyroxene

The clinopyroxenes in P-12 occur as: (1) Euhedral-to-subhedral phenocrysts and microphenocrysts (Fig. 4a, b); (2) small anhedral aggregates in the groundmass (Figs. 4b and 6b); (3) clusters of fine grained acicular crystals forming aggregates in the cores and rims of olivine (Fig. 3d); (4) cores of richterite crystals (Fig. 4c); (5) small acicular crystals at the margins of the carbonate clasts. The euhedral-to-subhedral phenocrysts and microphenocrysts are commonly rimmed by serpentine and chlorite. Similar serpentine and chlorite alteration is common within the pyroxene crystals (Fig. 4a, b). The groundmass pyroxenes are principally small (<30 μm) subhedral-to-anhedral crystals (Fig. 4b). The pyroxenes which form as a replacement product of olivine are patchy, very fine grained, and acicular in texture and associated with serpentine and chlorite (Fig. 3d). The pyroxenes which form the cores of richterites are prismatic and poikilitic with inclusions of hydrogarnet and chlorite (Fig. 4c). Pyroxene also occurs in the carbonate clasts in the form of square-to-wedge-shaped crystals completely surrounded by fine grained hydrogarnet-like material (Figs. 4d and 5a, b).

Representative compositions of pyroxenes of the various paragenetic types are given in Table 2. These do not differ significantly in their composition and are diopsides with only minor variation in their $TiO_2$, $Al_2O_3$, $Na_2O$ contents (Table 2). The phenocrystal and microphenocrystal pyroxenes are devoid of $Na_2O$ and $TiO_2$ and have low $FeO_T$ (<4.6 wt.%) contents (Table 2). The compositions of pyroxenes which form as a result of alteration of olivine are analogous to the compositions of the phenocrysts and microphenocrysts (Table 2). The pyroxenes forming cores of richterite crystals and the groundmass pyroxenes are enriched in $Na_2O$ (0.8–2.3 wt.%), $TiO_2$ (up to 2.8 wt.%), and $FeO_T$ (2.7–9.4 wt.%; Table 2). The pyroxene present in the carbonate clasts and surrounded by hydrogarnet material contain $Na_2O$ (0.6–0.8 wt.%) and $FeO_T$ (2.81–4.23 wt.%) and are similar in composition to pyroxene forming the cores of richterite and those in the groundmass (Table 2).

The groundmass subhedral-to-anhedral pyroxenes, pyroxenes in the cores of richterite crystals, and the euhedral pyroxenes present in carbonate material are the most evolved (Table 2) of the parageneses described above. These evolved pyroxenes exhibit subtle differences in terms of their $Na_2O$, CaO, FeO, and $TiO_2$ contents relative to the phenocryst/microphenocryst and acicular types. The Ti vs. Al diagram

**Table 1** Representative compositions (wt.%) of olivine

| | 1 | 2 | 3 | 4 | 5 | 6 | 7C | 7R | 8C | 8R | 9C | 9R | 10C | 10R | 11C | 11R | 12C | 12R | 13C | 13R |
|---|---|---|---|---|---|---|---|---|---|---|---|---|---|---|---|---|---|---|---|---|
| $SiO_2$ | 40.16 | 40.02 | 39.89 | 40.98 | 41.16 | 40.48 | 38.76 | 40.25 | 40.54 | 40.93 | 39.59 | 39.99 | 40.48 | 40.47 | 40.80 | 39.68 | 40.14 | 39.70 | 38.74 | 40.10 |
| $FeO_T$ | 13.76 | 13.88 | 12.84 | 13.05 | 7.91 | 13.83 | 18.90 | 14.07 | 7.76 | 11.83 | 16.46 | 14.34 | 13.45 | 14.02 | 7.49 | 14.94 | 13.59 | 15.15 | 18.50 | 14.47 |
| MnO | n.d. | n.d. | n.d. | n.d. | n.d. | n.d. | n.d. | 0.30 | n.d. | n.d. | 0.23 | 0.19 | n.d. | 0.22 | n.d. | 0.22 | n.d. | n.d. | 0.18 | 0.19 |
| MgO | 46.46 | 46.14 | 46.50 | 47.59 | 51.08 | 46.54 | 42.38 | 45.82 | 51.62 | 47.58 | 44.49 | 45.60 | 46.00 | 45.45 | 51.50 | 45.91 | 46.28 | 45.12 | 42.69 | 45.58 |
| CaO | 0.28 | 0.26 | 0.29 | n.d. | n.d. | n.d. | n.d. | n.d. | n.d. | n.d. | 0.15 | n.d. | 0.19 | 0.21 | 0.16 | 0.16 | n.d. | 0.18 | n.d. | 0.16 |
| NiO | n.d. | n.d. | n.d. | n.d. | 0.46 | n.d. | n.d. | n.d. | 0.34 | n.d. | n.d. | n.d. | 0.35 | n.d. | 0.33 | n.d. | 0.31 | n.d. | n.d. | n.d. |
| Total | 100.66 | 100.30 | 99.52 | 101.62 | 100.61 | 100.85 | 100.04 | 100.44 | 100.26 | 100.34 | 100.92 | 100.12 | 100.47 | 100.37 | 100.28 | 100.91 | 100.32 | 100.15 | 100.11 | 100.50 |
| Structural formula calculated on the basis of 4 oxygens | | | | | | | | | | | | | | | | | | | | |
| Si | 0.995 | 0.996 | 0.996 | 1.001 | 0.995 | 1.000 | 0.991 | 1.001 | 0.984 | 1.006 | 0.992 | 0.999 | 1.004 | 1.007 | 0.989 | 0.988 | 0.998 | 0.995 | 0.989 | 0.999 |
| Fe | 0.285 | 0.289 | 0.268 | 0.266 | 0.160 | 0.286 | 0.404 | 0.293 | 0.158 | 0.243 | 0.345 | 0.300 | 0.279 | 0.292 | 0.152 | 0.311 | 0.283 | 0.318 | 0.395 | 0.301 |
| Mn | – | – | – | – | – | – | – | 0.006 | – | – | 0.005 | 0.004 | – | 0.005 | – | 0.005 | – | – | 0.004 | 0.004 |
| Mg | 1.717 | 1.712 | 1.731 | 1.732 | 1.841 | 1.714 | 1.615 | 1.699 | 1.868 | 1.744 | 1.662 | 1.698 | 1.701 | 1.685 | 1.860 | 1.704 | 1.715 | 1.687 | 1.624 | 1.693 |
| Ca | 0.007 | 0.007 | 0.008 | – | – | – | – | – | – | – | 0.004 | – | 0.005 | 0.006 | 0.004 | 0.004 | – | 0.005 | – | 0.004 |
| Ni | – | – | – | – | – | – | – | – | 0.007 | – | – | – | 0.007 | – | 0.006 | – | 0.006 | – | – | – |
| $Mg^{\#}$ | 0.858 | 0.856 | 0.866 | 0.867 | 0.920 | 0.857 | 0.800 | 0.853 | 0.922 | 0.878 | 0.828 | 0.850 | 0.859 | 0.852 | 0.925 | 0.846 | 0.859 | 0.841 | 0.804 | 0.849 |

$Mg^{\#}$ = Mg/(Mg+Fe)

$FeO_T$ total Fe expressed as FeO

*C* core, *R* rim, *n.d.* not detected (<0.15 wt.%)

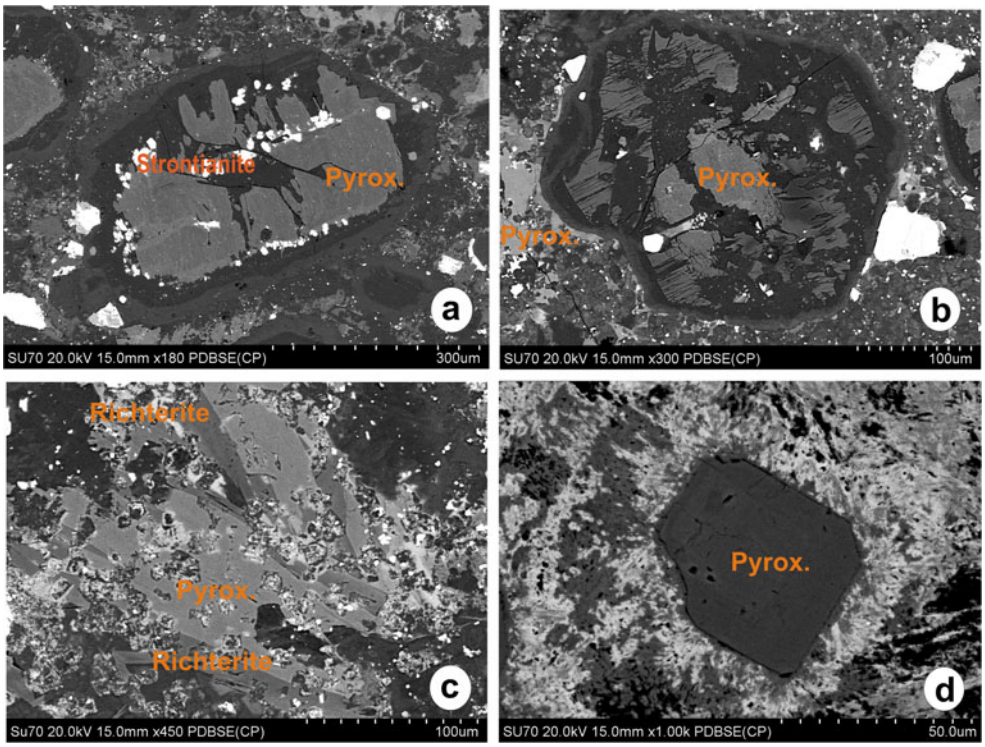


**Fig. 4** **a** Pyroxene with an alteration rim of serpentine. Small strontianite globules are seen in the pyroxene crystal (BSE image). **b** Altered euhedral pyroxene microphenocryst and fine grained groundmass pyroxene (BSE image). **c** Prismatic pyroxene in the core of richterite (BSE image). **d** Euhedral pyroxene surrounded by hydrogarnet material. (BSE image)

for all five varieties of pyroxene clearly indicates their lamproitic affinity (Fig. 10).

Mitchell and Bergman (1991) described clinopyroxenes from lamproites in three different parageneses: (1) phenocrysts and groundmass crystals of diopside; (2) green salites occurring as single crystals mantled by diopside, and as a major constituent of clinopyroxenite xenoliths; (3) colourless augites in olivine biotite pyroxenite inclusions in Leucite Hills lavas. The P-12 pyroxenes belong to paragenetic type 1 of Mitchell and Bergman (1991). Although the P-12 pyroxenes show $Na_2O$ enrichment up to 2.3 wt.%, the $Al_2O_3$ (<0.7 wt.%), and $TiO_2$ (<2.8 wt.%) contents are very similar

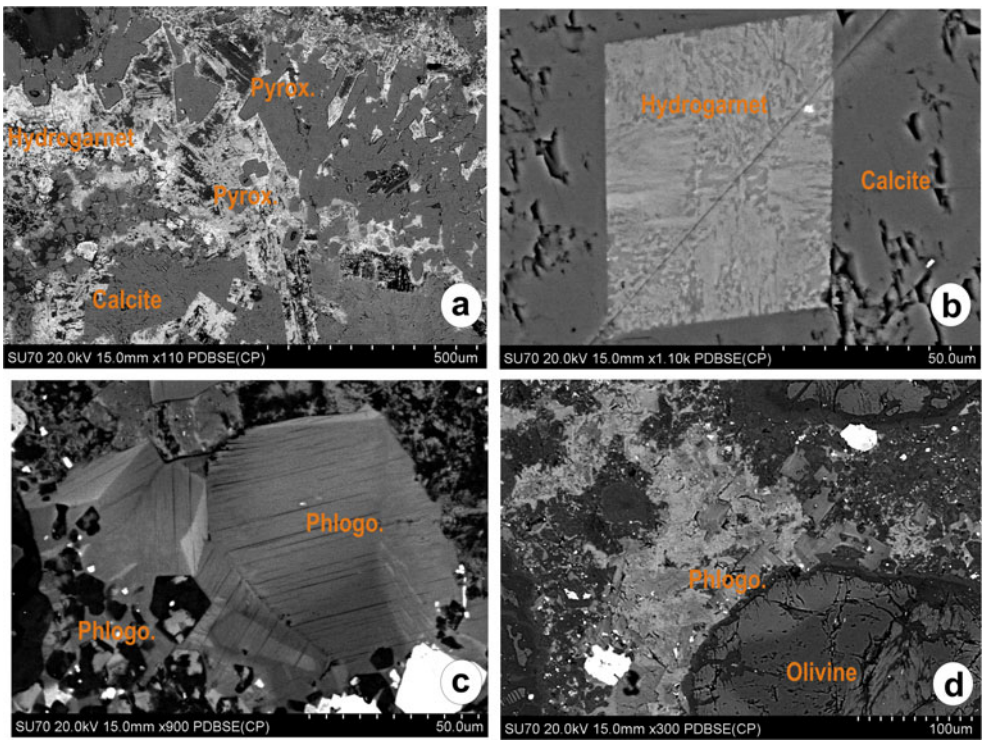


**Fig. 5** **a** Pyroxene crystals along with hydrogarnet material, cymrites and calcite (BSE image). **b** A relict euhedral hydrogarnet phase in calcite (BSE image). **c** Groundmass zoned phlogopites (poikilitic and platy) (BSE image). **d** Platy phlogopite formed at the rim of an olivine crystal. (BSE image)

**Table 2** Representative compositions (wt. %) of pyroxenes

| | 1 | 2 | 3 | 4 | 5 | 6 | 7 | 8 | 9 | 10 | 11 | 12 | 13 | 14 | 15 | 16 | 17 | 18 | 19 | 20 |
|---|---|---|---|---|---|---|---|---|---|---|---|---|---|---|---|---|---|---|---|---|
| $SiO_2$ | 55.57 | 55.62 | 54.38 | 55.10 | 54.22 | 52.02 | 54.00 | 53.27 | 53.28 | 53.46 | 53.65 | 52.69 | 53.92 | 54.31 | 54.74 | 55.31 | 55.57 | 55.62 | 55.28 | 54.96 |
| $TiO_2$ | n.d. | n.d. | n.d. | 0.46 | 1.50 | 1.13 | n.d. | n.d. | n.d. | 2.80 | 2.66 | 2.29 | 2.63 | n.d. | n.d. | n.d. | n.d. | n.d. | 0.41 | n.d. |
| $Al_2O_3$ | n.d. | n.d. | n.d. | 0.50 | 0.59 | 0.44 | 0.45 | 0.65 | 0.63 | 0.50 | 0.43 | 0.43 | 0.49 | n.d. | n.d. | n.d. | n.d. | n.d. | n.d. | 0.34 |
| $FeO_T$ | 3.78 | 3.49 | 4.62 | 3.80 | 3.73 | 4.71 | 9.37 | 7.13 | 6.72 | 5.18 | 5.44 | 5.22 | 5.13 | 4.93 | 3.80 | 4.11 | 3.78 | 3.49 | 3.99 | 4.21 |
| MnO | 0.32 | 0.19 | 0.32 | n.d. | n.d. | n.d. | n.d. | n.d. | n.d. | n.d. | n.d. | n.d. | n.d. | n.d. | n.d. | n.d. | n.d. | n.d. | n.d. | n.d. |
| MgO | 19.85 | 20.64 | 15.80 | 15.95 | 16.69 | 16.22 | 13.55 | 14.50 | 15.59 | 15.16 | 15.24 | 14.90 | 15.22 | 16.63 | 19.58 | 19.90 | 19.85 | 20.64 | 15.92 | 15.45 |
| CaO | 20.64 | 20.75 | 25.14 | 24.23 | 23.53 | 23.96 | 22.37 | 22.30 | 22.18 | 21.49 | 21.68 | 22.04 | 21.86 | 24.08 | 20.02 | 20.53 | 20.64 | 20.75 | 24.52 | 24.01 |
| $Na_2O$ | n.d. | n.d. | n.d. | 0.95 | 1.10 | 0.82 | 1.78 | 1.69 | 1.39 | 2.26 | 2.26 | 1.77 | 2.21 | n.d. | n.d. | n.d. | n.d. | n.d. | 0.73 | 0.82 |
| Total | 100.16 | 100.69 | 100.26 | 100.99 | 101.36 | 99.30 | 101.52 | 99.54 | 99.79 | 100.85 | 101.36 | 99.34 | 101.46 | 99.95 | 98.14 | 99.85 | 99.84 | 100.50 | 100.85 | 99.79 |
| Structural formula based on 6 atoms of oxygen | | | | | | | | | | | | | | | | | | | | |
| Si | 2.000 | 1.990 | 2.000 | 1.996 | 1.960 | 1.937 | 1.994 | 1.988 | 1.978 | 1.954 | 1.954 | 1.958 | 1.958 | 1.995 | 2.011 | 2.003 | 2.008 | 1.996 | 2.007 | 2.016 |
| Ti | – | – | – | 0.013 | 0.041 | 0.032 | – | – | – | 0.077 | 0.073 | 0.064 | 0.072 | – | – | – | – | – | 0.011 | – |
| Al | – | – | – | 0.021 | 0.025 | 0.019 | 0.020 | 0.029 | 0.028 | 0.022 | 0.018 | 0.019 | 0.021 | – | – | – | – | – | – | 0.015 |
| Fe | 0.110 | 0.100 | 0.140 | 0.115 | 0.113 | 0.147 | 0.289 | 0.222 | 0.209 | 0.158 | 0.166 | 0.162 | 0.156 | 0.151 | 0.117 | 0.124 | 0.114 | 0.105 | 0.121 | 0.129 |
| Mn | 0.010 | 0.010 | 0.010 | – | – | – | – | – | – | – | – | – | – | – | – | – | – | – | – | – |
| Mg | 1.070 | 1.100 | 0.860 | 0.861 | 0.899 | 0.901 | 0.746 | 0.807 | 0.863 | 0.826 | 0.827 | 0.825 | 0.824 | 0.911 | 1.072 | 1.074 | 1.070 | 1.104 | 0.862 | 0.845 |
| Ca | 0.800 | 0.800 | 0.990 | 0.941 | 0.911 | 0.956 | 0.885 | 0.892 | 0.882 | 0.842 | 0.846 | 0.877 | 0.851 | 0.948 | 0.788 | 0.796 | 0.799 | 0.798 | 0.954 | 0.944 |
| Na | – | – | – | 0.067 | 0.077 | 0.059 | 0.127 | 0.122 | 0.100 | 0.160 | 0.160 | 0.128 | 0.156 | – | – | – | – | – | 0.051 | 0.058 |

1–3: phenocrysts, microphenocrysts; 4–9: groundmass; 10–13:in cores of richterites; 14–18: altered after olivine; 19–20: in carbonate material

$FeO_T$ total Fe expressed as FeO

*n.d.* not detected (<0.15 wt.%)

to Leucite Hills, Smoky Butte, and Prairie Creek type 1 lamproite pyroxenes (Mitchell and Bergman 1991).

The P-12 pyroxenes have limited and subtle inter-grain compositional variation; a feature common in lamproite pyroxene. The absence of significant zoning and the limited intra-grain compositional variation could be caused by either rapid crystallization of the magma after pyroxene crystallization and/or its early replacement as a liquidus phase by amphibole (Mitchell and Bergman 1991). The acicular pyroxene forming after olivine in the macrocrysts, phenocrysts, and microphenocrysts of olivine, and the euhedral-to-subhedral pyroxenes in the carbonate clasts with hydrogarnet rims, are unique to P-12 and have not been described previously from lamproite rocks.

## Phlogopite

Phlogopite in P-12, commonly occurs as groundmass poikilitic plates and rarely as microphenocrysts (Fig. 5d). The poikilitic phlogopites have inclusions of spinel, pyroxene, apatite and chlorite. Phlogopite is also observed at the outer margins of olivine crystals, forming euhedral prismatic plates up to 30 microns in size (Fig. 5c). Alteration of phlogopite to chlorite is common.

Representative compositions of phlogopite are given in Table 3. The phlogopites from all the three paragenetic varieties have similar compositions (Table 3). They are deficient in $Al_2O_3$ (2.2–4.8 wt.%) and enriched in $TiO_2$ (1.1–4.6 wt.%), $Na_2O$ (0.4–2.7 wt.%), and $FeO_T$ (6.9–16 wt.%) with fluorine contents up to 6 wt.%.

Mitchell and Bergman (1991) reported five parageneses of phlogopite in lamproites: (1) phenocrysts; (2) groundmass poikilitic plates; (3) mantled micas; (4) phlogopite pyroxenite and phlogopite inclusions; (5) coronas around olivine and rarely chromite. In P-12, phlogopites from three of these parageneses have been observed: poikilitic groundmass phlogopites; microphenocrysts; and phlogopites forming as rims on olivine. All of the phlogopites are sodic titanian tetraferriphlogopites (Table 3) similar in composition to those occurring in lamproites (Mitchell and Bergman 1991). Such phlogopites represent one of the most sodic phases found in lamproites (Mitchell and Bergman 1991). The $Al_2O_3$ contents of P-12 phlogopites are extremely low (<5 wt.%; Table 3), and thus lower than the range of 5–11 wt.% $Al_2O_3$ reported for other lamproite phlogopites (Kuehner 1980; Mitchell 1981, 1989; Jaques et al. 1986; Scott Smith et al. 1989; Mitchell and Bergman 1991; Fritschle et al. 2013; Gurmeet Kaur and Mitchell 2013). Compositions of the phlogopites which rim

**Table 3** Representative compositions (wt. %) of phlogopites

| | 1 | 2 | 3 | 4 | 5 | 6 | 7 | 8 | 9 | 10 | 11 | 12 | 13 | 14 | 15 | 16 | 17 | 18C | 18R |
|---|---|---|---|---|---|---|---|---|---|---|---|---|---|---|---|---|---|---|---|
| $SiO_2$ | 44.32 | 45.55 | 43.58 | 46.65 | 45.65 | 43.26 | 44.90 | 43.67 | 46.41 | 43.79 | 46.94 | 45.86 | 42.99 | 43.08 | 45.90 | 45.39 | 46.29 | 43.89 | 47.30 |
| $TiO_2$ | 3.49 | 3.23 | 2.95 | 2.68 | 3.23 | 3.64 | 1.88 | 2.88 | 2.41 | 4.55 | 2.13 | 3.51 | 3.90 | 1.11 | 1.97 | 1.60 | 2.25 | 4.41 | 2.98 |
| $Al_2O_3$ | 2.83 | 2.79 | 2.24 | 2.30 | 2.43 | 2.58 | 2.84 | 3.19 | 2.68 | 2.55 | 2.76 | 3.83 | 3.21 | 4.83 | 2.63 | 3.72 | 2.59 | 2.86 | 2.66 |
| $FeO_T$ | 12.86 | 12.52 | 12.93 | 8.36 | 11.01 | 12.01 | 11.34 | 11.80 | 8.98 | 15.97 | 6.95 | 9.42 | 10.89 | 10.05 | 10.13 | 10.01 | 10.00 | 11.70 | 9.51 |
| MgO | 21.26 | 22.23 | 21.08 | 22.19 | 21.50 | 21.72 | 22.21 | 21.06 | 22.27 | 19.59 | 22.01 | 23.70 | 21.18 | 23.96 | 23.29 | 23.05 | 22.73 | 21.41 | 22.21 |
| $Na_2O$ | 1.35 | 0.97 | 1.88 | 2.69 | 2.15 | 1.46 | 1.63 | 1.68 | 1.86 | 0.43 | 2.50 | 0.94 | 0.80 | 1.30 | 2.03 | 1.59 | 0.58 | 1.69 | 2.63 |
| $K_2O$ | 9.72 | 9.95 | 9.81 | 10.20 | 9.52 | 9.21 | 9.94 | 9.50 | 9.67 | 9.24 | 9.82 | 9.33 | 9.02 | 9.57 | 9.83 | 9.82 | 9.51 | 9.31 | 10.14 |
| BaO | 1.30 | 1.46 | 1.40 | n.d. | 1.37 | 2.46 | 0.97 | 1.61 | 0.99 | 2.05 | n.d. | n.d. | 2.01 | 1.29 | 1.13 | 0.91 | 0.79 | 2.75 | 1.18 |
| F | 1.84 | 0.90 | 2.65 | 5.98 | 4.11 | 1.83 | 2.18 | 4.21 | 2.95 | n.d. | 5.13 | n.d. | n.d. | 2.94 | 4.36 | 2.53 | 5.26 | 4.42 | 5.00 |
| Total | 98.20 | 99.22 | 97.40 | 98.53 | 99.24 | 97.40 | 96.97 | 97.83 | 96.98 | 98.17 | 96.08 | 96.59 | 94.00 | 95.19 | 96.91 | 96.09 | 94.74 | 98.02 | 98.61 |
| Structural formula calculated on the basis of 16 cations | | | | | | | | | | | | | | | | | | | |
| Si | 6.550 | 6.624 | 6.493 | 6.806 | 6.698 | 6.468 | 6.623 | 6.538 | 6.849 | 6.597 | 6.967 | 6.674 | 6.599 | 6.326 | 6.641 | 6.622 | 6.932 | 6.472 | 6.743 |
| Ti | 0.388 | 0.353 | 0.331 | 0.294 | 0.356 | 0.409 | 0.209 | 0.324 | 0.267 | 0.515 | 0.238 | 0.384 | 0.450 | 0.123 | 0.214 | 0.176 | 0.253 | 0.489 | 0.319 |
| Al | 0.493 | 0.478 | 0.393 | 0.395 | 0.420 | 0.455 | 0.494 | 0.563 | 0.466 | 0.453 | 0.483 | 0.657 | 0.581 | 0.836 | 0.448 | 0.640 | 0.457 | 0.497 | 0.447 |
| Fe | 1.590 | 1.523 | 1.611 | 1.020 | 1.351 | 1.502 | 1.399 | 1.477 | 1.108 | 2.012 | 0.863 | 1.146 | 1.398 | 1.234 | 1.226 | 1.221 | 1.252 | 1.443 | 1.134 |
| Mg | 4.684 | 4.819 | 4.682 | 4.826 | 4.703 | 4.842 | 4.884 | 4.701 | 4.899 | 4.400 | 4.870 | 5.142 | 4.847 | 5.245 | 5.023 | 5.013 | 5.074 | 4.706 | 4.720 |
| Na | 0.387 | 0.273 | 0.543 | 0.761 | 0.612 | 0.423 | 0.466 | 0.488 | 0.532 | 0.126 | 0.719 | 0.265 | 0.238 | 0.370 | 0.569 | 0.450 | 0.168 | 0.483 | 0.727 |
| K | 1.833 | 1.846 | 1.865 | 1.898 | 1.782 | 1.757 | 1.870 | 1.815 | 1.821 | 1.776 | 1.860 | 1.732 | 1.766 | 1.793 | 1.814 | 1.828 | 1.817 | 1.751 | 1.844 |
| Ba | 0.075 | 0.083 | 0.082 | – | 0.079 | 0.144 | 0.056 | 0.094 | 0.057 | 0.121 | – | – | 0.121 | 0.074 | 0.064 | 0.052 | 0.046 | 0.159 | 0.066 |
| F | 0.860 | 0.414 | 1.249 | 2.759 | 1.907 | 0.865 | 1.017 | 1.993 | 1.377 | – | 2.408 | – | – | 1.365 | 1.995 | 1.167 | 2.491 | 2.061 | 2.254 |

1–13: Poikilitic groundmass phlogopites; 14–17: phlogopite mantling olivine crystals; 18C-18R: Core and Rim of Microphenocryst

$FeO_T$total Fe expressed as FeO

*n.d.* not detected (<0.15 wt.%)

olivine are identical to those of microphenocryst and the groundmass poikilitic mica. The fluorine (up to 6 wt.%) and BaO (up to 2.7 wt.%) contents are similar to those of phlogopite in lamproites (Jaques et al. 1986; Scott Smith and Skinner 1984; Kuehner et al. 1981; Foley et al. 1986; Mitchell and Bergman 1991; Fritschle et al. 2013). The compositional evolution shown by the phlogopites follows a lamproitic trend (Fig. 11a, b). Ba-rich micas characteristic of *bona fide* kimberlites are not present.

## Amphiboles

The amphibole present in P-12 occurs as groundmass poikilitic plates and small euhedral-to-subhedral crystals. The plates range up to 200 μm in size and typically contain inclusions of diopside, apatite, and hydrogarnet (Figs. 4c and 6a, b). In some instances, the amphiboles rim diopside crystals (Fig. 4c). The small crystals (<30 μm) are primarily wedge-shaped (Fig. 6b) and commonly found at the margins of olivine and pyroxene crystals. The poikilitic groundmass amphiboles are patchily-zoned whereas the small euhedral crystals are not zoned. Inter-grain variation has been observed in $TiO_2$ and $FeO_T$ (Table 4).

Representative compositions of the amphiboles are given in Table 4. All have low $Al_2O_3$ (<1.5 wt.%) contents typical of most lamproite amphibole (Mitchell and Bergman 1991). The $Al_2O_3$ (<1.5 wt.%), $TiO_2$ (>2 wt.%), $Na_2O$ (4.3–4.8 wt.%), $K_2O$ (4.2–4.6 wt.%), $FeO_T$ (1.3–9.4 wt.%), and fluorine contents up to 3.8 wt.% are similar to those of amphiboles from the Leucite Hills; Smoky Butte; West Kimberly; and Murcia-Almeria lamproites (Wagner and Velde 1986; Mitchell and Bergman 1991). The low Al and Ti contents (Table 4) of the P-12 amphiboles results in a tetrahedral site deficiency as [(Si+Al+Ti)<8]. This can be remedied only if $Fe^{3+}$ also occupies this site (Hogarth 1997). Most of the amphiboles from P-12 have Na in excess of K at the A-site (Table 4), in common with Leucite Hills amphiboles (Mitchell and Bergman 1991).

The Si vs. Mg/(Mg+$Fe^{2+}$) binary classification diagram for sodic-calcic amphiboles after Leake et al. (1997), indicates that P-12 amphiboles are titanian potassium richterites and titanian potassium magnesio-katophorites (Fig. 12). There is a clear evolutionary trend of amphibole compositions from titanian potassium magnesium katophorite to titanian potassium richterite (Fig. 12).

The extremely low $Al_2O_3$ content of the amphiboles is attributed to the low alumina contents of their parental peralkaline magma (Wagner and Velde 1986; Mitchell and Bergman 1991). Figures 13 and 14 clearly demonstrate the affinity of P12 amphiboles with those found in the West Kimberley and Smoky Butte lamproites (Mitchell and Bergman 1991).

## Perovskite

Perovskite occurs principally in two parageneses, as small (<20 μm) euhedral crystals dispersed throughout the groundmass or as inclusions in olivine phenocrysts/

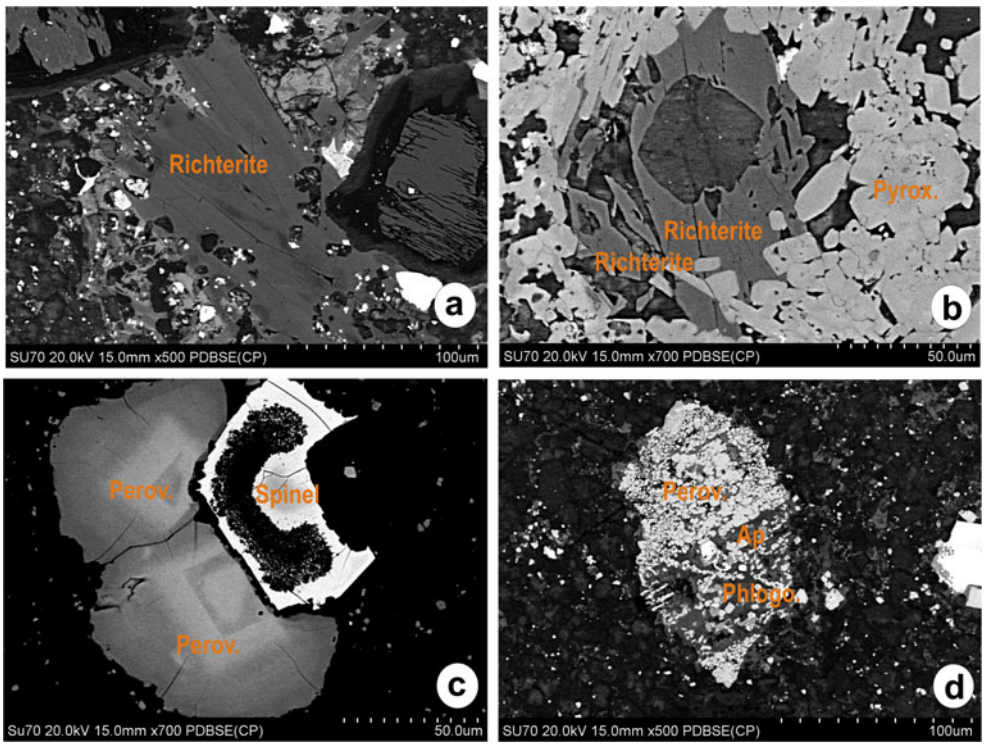


**Fig. 6** **a** Groundmass poikilitic richterite plate (BSE image). **b** Wedge-shaped richterite crystals surrounded by fine grained pyroxene crystals (BSE image). **c** Multiple zoned perovskites with atoll spinel (BSE image). **d** A microclast of phlogopite and apatite with numerous small euhedral perovskites (BSE image)

**Table 4** Representative compositions (wt. %) of amphiboles

| | 1 | 2 | 3 | 4 | 5 | 6 | 7 | 8 | 9 | 10 | 11 | 12 | 13 | 14 |
|---|---|---|---|---|---|---|---|---|---|---|---|---|---|---|
| $SiO_2$ | 53.82 | 52.41 | 52.31 | 55.72 | 53.65 | 50.26 | 51.89 | 49.66 | 49.71 | 49.17 | 48.91 | 48.37 | 48.40 | 55.60 |
| $TiO_2$ | 2.14 | 2.37 | 2.61 | 0.34 | 1.96 | 4.97 | 2.83 | 5.62 | 4.65 | 4.80 | 5.57 | 6.24 | 5.72 | 1.92 |
| $Al_2O_3$ | 1.27 | 1.33 | 1.45 | 0.23 | 1.08 | 1.06 | 0.53 | 1.12 | 1.31 | 1.41 | 1.18 | 2.25 | 1.39 | 1.09 |
| $Fe_2O_3$ | 3.71 | 2.91 | 2.21 | 1.72 | 3.99 | 3.26 | 4.05 | 3.65 | 5.42 | 3.96 | 3.73 | 1.63 | 4.05 | 0.94 |
| FeO | 1.32 | 3.56 | 2.90 | 3.43 | 1.22 | 5.79 | 5.76 | 4.98 | 3.12 | 3.26 | 5.45 | 6.53 | 4.16 | 0.44 |
| MgO | 21.84 | 19.89 | 20.91 | 21.00 | 21.32 | 18.30 | 18.35 | 18.76 | 19.75 | 18.97 | 17.59 | 18.10 | 18.56 | 23.52 |
| CaO | 6.47 | 5.97 | 6.48 | 6.22 | 6.15 | 5.69 | 6.34 | 5.99 | 6.00 | 6.40 | 5.99 | 5.96 | 5.92 | 6.47 |
| $Na_2O$ | 4.53 | 4.52 | 4.35 | 4.69 | 4.83 | 4.73 | 4.53 | 4.63 | 4.64 | 4.61 | 4.80 | 4.28 | 4.69 | 4.69 |
| $K_2O$ | 4.56 | 4.54 | 4.26 | 4.34 | 4.40 | 4.42 | 4.46 | 4.42 | 4.19 | 4.21 | 4.29 | 4.45 | 4.19 | 4.31 |
| Total | 99.66 | 97.50 | 97.48 | 97.69 | 98.60 | 98.49 | 98.74 | 98.83 | 98.79 | 96.79 | 97.51 | 97.81 | 97.09 | 98.97 |
| F | 2.80 | 3.35 | 3.58 | 3.32 | 3.43 | 3.78 | 3.41 | 3.56 | 3.51 | 3.37 | 3.36 | 2.85 | 3.55 | 3.69 |
| Structural formula calculated on the basis of 16 cations | | | | | | | | | | | | | | |
| Si | 7.494 | 7.519 | 7.469 | 7.889 | 7.545 | 7.262 | 7.471 | 7.151 | 7.123 | 7.179 | 7.161 | 7.052 | 7.084 | 7.670 |
| Ti | 0.224 | 0.256 | 0.280 | 0.036 | 0.207 | 0.540 | 0.307 | 0.609 | 0.501 | 0.527 | 0.614 | 0.684 | 0.630 | 0.199 |
| Al | 0.208 | 0.225 | 0.244 | 0.038 | 0.179 | 0.181 | 0.090 | 0.190 | 0.221 | 0.243 | 0.204 | 0.387 | 0.240 | 0.177 |
| $Fe^{3+}$ | 0.389 | 0.315 | 0.237 | 0.183 | 0.423 | 0.355 | 0.438 | 0.395 | 0.585 | 0.435 | 0.411 | 0.179 | 0.447 | 0.097 |
| $Fe^{2+}$ | 0.154 | 0.427 | 0.347 | 0.407 | 0.143 | 0.700 | 0.693 | 0.599 | 0.374 | 0.398 | 0.668 | 0.797 | 0.509 | 0.050 |
| Mg | 4.533 | 4.254 | 4.451 | 4.432 | 4.470 | 3.942 | 3.939 | 4.027 | 4.219 | 4.129 | 3.839 | 3.934 | 4.049 | 4.837 |
| Ca | 0.965 | 0.918 | 0.991 | 0.944 | 0.927 | 0.881 | 0.978 | 0.924 | 0.921 | 1.001 | 0.940 | 0.931 | 0.928 | 0.956 |
| Na | 1.223 | 1.257 | 1.204 | 1.287 | 1.317 | 1.325 | 1.265 | 1.293 | 1.289 | 1.305 | 1.363 | 1.210 | 1.331 | 1.254 |
| K | 0.810 | 0.831 | 0.776 | 0.784 | 0.789 | 0.815 | 0.819 | 0.812 | 0.766 | 0.784 | 0.801 | 0.828 | 0.782 | 0.758 |
| Total | 16.00 | 16.00 | 16.00 | 16.00 | 16.00 | 16.00 | 16.00 | 16.00 | 16.00 | 16.00 | 16.00 | 16.00 | 16.00 | 16.00 |
| T site = Si+Al+Ti | 7.926 | 7.999 | 7.994 | 7.963 | 7.931 | 7.983 | 7.868 | 7.950 | 7.846 | 7.948 | 7.978 | 8.000 | 7.953 | 8.000 |
| C site = Ti+$Fe^{3+}$+$Fe^{2+}$+Mg | 5.076 | 4.995 | 5.035 | 5.022 | 5.036 | 4.997 | 5.071 | 5.022 | 5.178 | 4.961 | 4.918 | 5.032 | 5.005 | 5.030 |
| B site = Ca+Na | 2.000 | 2.000 | 2.000 | 2.000 | 2.000 | 2.000 | 2.000 | 2.000 | 2.000 | 2.000 | 2.000 | 2.000 | 2.000 | 2.000 |
| A site = Na+K | 0.998 | 1.006 | 0.972 | 1.015 | 1.033 | 1.021 | 1.062 | 1.029 | 0.976 | 1.090 | 1.104 | 0.968 | 1.041 | 0.969 |

$Fe_2O_3$ and FeO calculated on a stoichiometric basis

microphenocrysts, and as large (100 to 300 μm) subhedral-to-euhedral, oscillatory-zoned crystals associated with spinels (Figs. 6c and 7a, b). A third variety of crystals (1 to 10 μm) occurs in phlogopite and apatite micro-clasts (Fig. 6d).

Representative compositions of perovskites are given in Tables 5 and 6. Perovskites in the micro-clasts were too small to analyse. All perovskites in P-12 are only slightly enriched in LREEs in common with other lamproite perovskites (Jaques et al. 1986; Mitchell and Reed 1988; Mitchell and Bergman 1991; Mitchell 2002; Gurmeet Kaur and Mitchell 2013; Gurmeet Kaur et al. 2013). The cores of the zoned perovskites are more enriched in the REEs ($La_2O_3$: 1.5–2.6 wt.%; $Ce_2O_3$: 2.7–3.4 wt.%; $Nd_2O_3$: 1.2–1.7 wt.%), $Nb_2O_5$ (0.6–1.0 wt.%), $Na_2O$ (0.8–1.0 wt.%) relative to the rims ($La_2O_3$: 1.3–1.7 wt.%; $Ce_2O_3$: 1.4–2.5 wt.%; $Nd_2O_3$: 0.6–1.4 wt.%), $Nb_2O_5$ (0.5–0.8 wt.%), $Na_2O$ (0.4–0.8 wt.%). The zonation-free perovskites have REE contents ($La_2O_3$: 1.1–1.7 wt.%; $Ce_2O_3$: 0.9–2.4 wt.%; $Nd_2O_3$: 0.5–0.9 wt.%), $Na_2O$ (0.5–1.0 wt.%) similar to the rims of the zoned perovskites, indicating crystallization contemporaneous with the rim parts of the zoned perovskites (Table 5).

The oscillatory-zoned perovskites typically exhibit three-or-more compositionally-distinct zones (Table 6). Normal and reverse oscillatory zoning with respect to REEs have been noted (Table 6). The oscillatory-zoned perovskites exhibit normal oscillatory zoning with higher LREEs in the core; decrease in LREEs in the first zone, increase in LREEs in the second zone and decrease in LREEs in the third zone (comps. 1–4; Table 6). Some perovskites show reverse oscillatory zoning i.e., low LREEs in the core; an increase in the first zone, and a decrease in the second zone (comps. 5–7, 8–9; Table 6).

Slight REE enrichment and low $FeO_T$ (up to 1.8 wt.%) contents of these perovskites do not permit assignment to either a lamproite or kimberlite parentage. However, P-12 perovskites are poor in strontium in contrast to most lamproite perovskites (Mitchell and Bergman 1991).

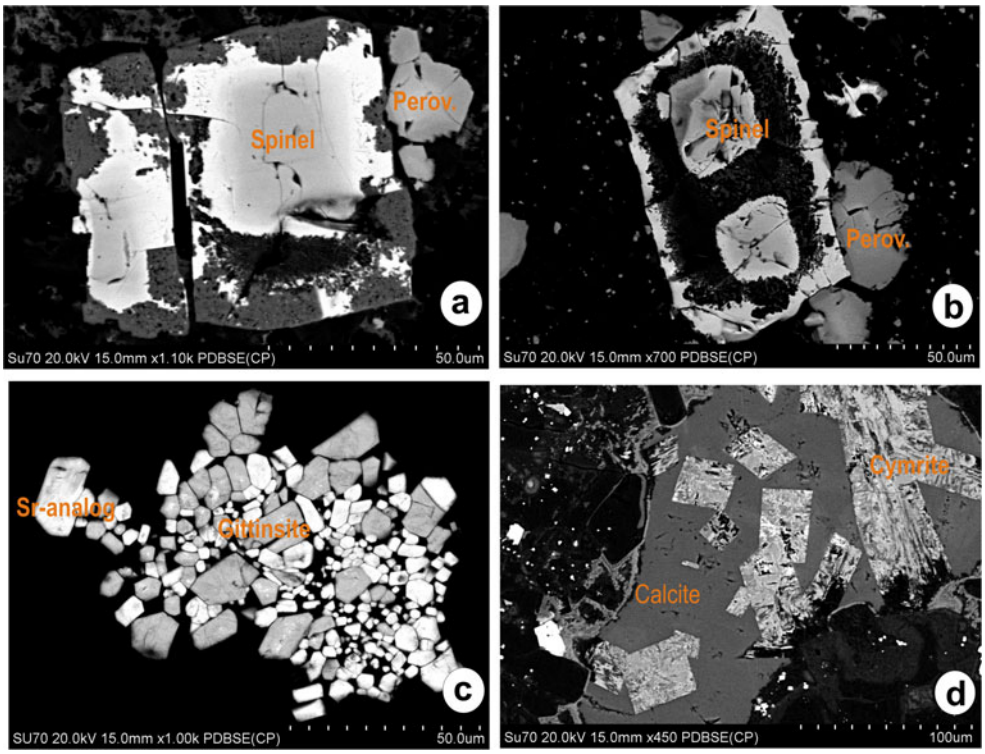


**Fig. 7** **a** Relict zoned spinel and perovskite (BSE image). **b** Double core atoll spinel (BSE image). **c** Euhedral gittinsite (*dark grey*) and the strontium analog of gittinsite (*light grey*) in groundmass material (BSE image). **d** Cymrites and cymrite relicts in carbonate material (BSE image)

## Spinels

Spinels are present in P-12 as euhedral-to-subhedral atoll spinels, and small euhedral-to-subhedral groundmass spinels. Those which are larger than 50 μm are commonly atoll spinels with single and/or double cores (Figs. 6c and 7a, b). The atoll spinels are principally associated with perovskites (Figs. 6c and 7b, d). The small spinels (<5 to 50 μm) are randomly distributed throughout the groundmass and as inclusions in the core and rims of olivine crystals.

Representative compositions of atoll and groundmass spinels are given in Tables 7 and 8. The atoll spinels have cores rich in $Cr_2O_3$ (up to 53 wt.%) and MgO (up to 9.4 wt.%), and rims which are enriched in $FeO_T$ (up to 82.3 wt.%) and $TiO_2$ titanium (up to 10.9 wt.%). The $Al_2O_3$ contents of the cores are less than 8 wt.% and the rims are impoverished in $Al_2O_3$ (<1 wt.%). The atoll spinels have cores which correspond to titanian aluminous magnesiochromite (Group 2) and rims which correspond to magnesian titaniferous magnetites (Group 4) The groundmass spinels are ulvöspinels belonging to Group 4 of Mitchell and Bergman (1991) and are enriched in $FeO_T$ (up to 84.wt.%), $TiO_2$ (10.5 wt.%), and low in alumina (generally <1 wt.%). Spinel inclusions in the cores of olivine crystals are iron-rich magnetites, whereas those occurring in the rim of olivine crystals are chromium-rich (chrome spinels).

The spinel compositions of both parageneses are projected onto the front face of the reduced iron spinel compositional prism in Fig. 15. The atoll spinels and the groundmass spinels follow the lamproite spinel trend of Mitchell and Bergman (1991). As most of the spinels are poor in alumina they indicate the peralkaline nature of the magma from which they crystallized, and affinity to the lamproite clan of rocks.

Atoll spinels are characteristic of kimberlite rocks and are usually absent in lamproites (Mitchell and Bergman 1991). Atoll spinels have been reported from P-5 to P-13 lamproites from Wajrakarur-Lattavaram cluster (Gurmeet Kaur et al. 2013).

## Gittinsite and strontium zirconium silicate

Gittinsite ($CaZrSi_2O_7$), and a strontium analog ($SrZrSi_2O_7$), form rare euhedral-to-subhedral crystals varying in size from <1 to 25 μm (Fig. 7c). Neither gittinsite, nor $SrZrSi_2O_7$, have been previously recognized in any lamproite, and the latter is known only as a synthetic compound (Huntelaar et al. 1994). Both minerals are hosted by chloritic material together with apatite and calcite. Representative compositions of gittinsite and $SrZrSi_2O_7$ are given in Table 9.

Gittinsites have been reported from peralkaline granites and syenites in the Kipawa and Strange Lake complexes (Ansell et al. 1980; Birkett et al. 1992) and from carbonatites at the Afrikanda complex (Chakhmouradian and Zaitsev 2002). The occurrence of gittinsite indicates the peralkaline nature of the magma (Ansell et al. 1980; Birkett et al. 1992; Chakhmouradian and Zaitsev 2002).

**Table 5** Representative compositions (wt. %) of zoned and unzoned perovskites

| | 1C | 1R | 2C | 2R | 3C | 3R | 4C | 4R | 5C | 5R | 6C | 6R | 7 | 8 | 9 |
|---|---|---|---|---|---|---|---|---|---|---|---|---|---|---|---|
| $Nb_2O_5$ | 1.02 | 0.82 | 0.70 | 0.81 | 1.03 | 0.75 | 0.82 | 0.76 | 0.61 | 0.52 | 0.83 | 0.49 | 0.95 | 1.15 | 0.90 |
| $TiO_2$ | 52.29 | 54.17 | 52.29 | 53.64 | 52.51 | 52.80 | 53.25 | 53.54 | 53.30 | 54.86 | 51.13 | 52.55 | 53.58 | 55.32 | 54.81 |
| $ThO_2$ | 0.85 | n.d. | 1.05 | n.d. | 0.78 | n.d. | 1.03 | n.d. | n.d. | n.d. | 1.08 | 0.76 | n.d. | n.d. | n.d. |
| $Al_2O_3$ | 0.38 | 0.44 | n.d. | 0.47 | 0.35 | 0.36 | n.d. | n.d. | n.d. | n.d. | 0.43 | 0.39 | n.d. | n.d. | n.d. |
| $La_2O_3$ | 1.70 | 1.69 | 1.83 | 1.76 | 1.87 | 1.79 | 1.65 | 1.33 | 1.50 | 1.77 | 2.56 | 1.72 | 1.75 | 1.09 | 1.45 |
| $Ce_2O_3$ | 2.94 | 1.40 | 2.72 | 1.49 | 3.01 | 2.00 | 3.05 | 2.31 | 3.29 | 2.26 | 3.28 | 2.48 | 2.44 | 0.88 | 1.55 |
| $Nd_2O_3$ | 1.63 | 1.10 | 1.45 | 0.60 | 1.17 | 0.79 | 1.57 | 0.73 | 1.40 | 0.74 | 1.73 | 1.42 | 0.96 | 0.47 | 0.82 |
| $FeO_T$ | 1.50 | 1.40 | 1.58 | 1.77 | 1.45 | 1.32 | 1.29 | 1.35 | 1.49 | 1.59 | 1.42 | 1.58 | 1.37 | 1.23 | 1.64 |
| CaO | 33.74 | 37.40 | 34.24 | 37.23 | 34.54 | 36.20 | 34.99 | 36.91 | 35.58 | 37.89 | 34.11 | 34.63 | 35.54 | 36.01 | 36.80 |
| BaO | 1.33 | 1.53 | 1.98 | 1.24 | 1.74 | 1.89 | 1.70 | 1.04 | 1.56 | 1.09 | 2.32 | 1.19 | 1.60 | 1.38 | 1.17 |
| $Na_2O$ | 1.02 | 0.48 | 0.82 | 0.41 | 0.79 | 0.73 | 0.99 | 0.64 | 1.07 | 0.56 | 0.90 | 0.83 | 0.75 | 0.98 | 0.49 |
| Total | 98.40 | 100.43 | 98.66 | 99.42 | 99.24 | 98.63 | 100.34 | 98.61 | 99.80 | 101.28 | 99.79 | 98.04 | 98.94 | 98.51 | 99.63 |
| Structural formula based on 3 atoms of oxygen | | | | | | | | | | | | | | | |
| Na | 0.048 | 0.022 | 0.039 | 0.019 | 0.037 | 0.034 | 0.046 | 0.030 | 0.050 | 0.025 | 0.043 | 0.039 | 0.035 | 0.045 | 0.022 |
| Ca | 0.880 | 0.941 | 0.896 | 0.944 | 0.894 | 0.933 | 0.899 | 0.945 | 0.913 | 0.947 | 0.893 | 0.902 | 0.913 | 0.912 | 0.929 |
| Ba | 0.013 | 0.014 | 0.019 | 0.011 | 0.016 | 0.018 | 0.016 | 0.010 | 0.015 | 0.010 | 0.022 | 0.011 | 0.015 | 0.013 | 0.011 |
| La | 0.015 | 0.015 | 0.016 | 0.015 | 0.017 | 0.016 | 0.015 | 0.012 | 0.013 | 0.015 | 0.023 | 0.015 | 0.015 | 0.009 | 0.013 |
| Ce | 0.026 | 0.012 | 0.024 | 0.013 | 0.027 | 0.018 | 0.027 | 0.020 | 0.029 | 0.019 | 0.029 | 0.022 | 0.021 | 0.008 | 0.013 |
| Nd | 0.014 | 0.009 | 0.013 | 0.005 | 0.010 | 0.007 | 0.013 | 0.006 | 0.012 | 0.006 | 0.015 | 0.012 | 0.008 | 0.004 | 0.007 |
| Th | 0.005 | – | 0.006 | – | 0.004 | – | 0.006 | – | – | – | 0.006 | 0.004 | – | – | – |
| Total A | 1.001 | 1.012 | 1.013 | 1.007 | 1.006 | 1.025 | 1.021 | 1.023 | 1.031 | 1.023 | 1.031 | 1.006 | 1.008 | 0.990 | 0.995 |
| Ti | 0.958 | 0.957 | 0.961 | 0.955 | 0.955 | 0.955 | 0.960 | 0.963 | 0.960 | 0.962 | 0.940 | 0.961 | 0.967 | 0.983 | 0.972 |
| Fe | 0.031 | 0.027 | 0.032 | 0.035 | 0.029 | 0.027 | 0.026 | 0.027 | 0.030 | 0.031 | 0.029 | 0.032 | 0.027 | 0.024 | 0.032 |
| Al | 0.011 | 0.012 | – | 0.013 | 0.010 | 0.010 | – | – | – | – | 0.012 | 0.011 | – | – | – |
| Nb | 0.011 | 0.009 | 0.008 | 0.009 | 0.011 | 0.008 | 0.009 | 0.008 | 0.007 | 0.005 | 0.009 | 0.005 | 0.010 | 0.012 | 0.010 |
| Total B | 1.010 | 1.005 | 1.001 | 1.011 | 1.005 | 1.000 | 0.995 | 0.998 | 0.997 | 0.999 | 0.990 | 1.010 | 1.004 | 1.020 | 1.014 |

1–6: zoned perovskites; 7–9: unzoned perovskites

$FeO_T$ total Fe expressed as FeO

*C* core, *R* rim, *n.d.* not detected (<0.15 wt.%)

## Cymrite

Prismatic-to-tabular crystals of cymrite ($BaAl_2Si_2O_8.H_2O$) are found both in the carbonate clasts and the groundmass material of P-12. The crystals vary in size from 20 to 150 μm (Figs. 7d and 8a). The cymrite crystals are mostly associated with calcite, barite, pyroxene, and hydrogarnet (Figs. 7d and 8a, b). Representative compositions of cymrite, up to 2.3 wt.% CaO and 0.6 wt.% $K_2O$. are given in Table 10.

Cymrites have been reported to form under diverse pressure-temperature conditions in many geological environments (Runnells 1964; Essene 1967; Reinecke 1982; Moles 1985; Stankova et al. 1989; Jacobsen 1990; Hsu 1994; Moro et al. 2001; Sorokhtina et al. 2008; Raith et al. 2014). Reports of cymrite forming from celsian by hydration are documented for barite-bearing siliceous and carbonate rocks (Moro et al. 2001). Cymrite and celsian are related by the reaction:

$$BaAl_2Si_2O_8(\text{celsian}) + nH_2O = BaAl_2Si_2O_8 \cdot nH_2O(\text{cymrite}) \quad (1)$$

as demonstrated by Essene (1967), Reinecke (1982), and Moro et al. (2001). In contrast, Hsu (1994) suggested the formation of cymrite by the reaction:

$$BaSO_4 + 2OH^- + A1_2O_3 + 2SiO_2 = BaA1_2Si_2O_8.H_2O + SO_4{}^{2-} \quad (2)$$

The formation of cymrite in P-12 can be explained by either and/or both of the reactions described above. Thus, cymrite in P-12 could form by hydration of celsian ($BaAl_2Si_2O_8$) originally formed by replacement of potassium feldspar. Although potassium feldspars have not been preserved, this hypothesis is supported by the cymrite morphology which suggests formation after prismatic tabular crystals

**Table 6** Representative compositions (wt. %) of oscillatory zoned perovskites

| | 1 | 2 | 3 | 4 | 5 | 6 | 7 | 8 | 9 | 10 |
|---|---|---|---|---|---|---|---|---|---|---|
| $Nb_2O_5$ | 0.72 | 0.47 | 0.99 | 0.55 | 0.61 | 0.83 | 0.59 | 0.58 | 0.78 | 1.24 |
| $TiO_2$ | 51.73 | 53.29 | 52.23 | 52.73 | 53.83 | 52.28 | 54.74 | 54.46 | 53.27 | 55.58 |
| $ThO_2$ | 1.06 | 0.72 | 0.90 | n.d. | 0.37 | 0.49 | 0.36 | 0.49 | 0.80 | n.d. |
| $Al_2O_3$ | 0.42 | 0.27 | 0.33 | 0.28 | 0.35 | 0.24 | 0.42 | n.d. | n.d. | n.d. |
| $La_2O_3$ | 1.87 | 1.61 | 2.06 | 1.70 | 1.35 | 1.47 | 1.73 | 1.83 | 2.08 | 1.25 |
| $Ce_2O_3$ | 2.86 | 2.42 | 2.81 | 1.76 | 2.67 | 2.74 | 2.23 | 2.60 | 2.99 | 0.66 |
| $Nd_2O_3$ | 1.71 | 1.43 | 1.79 | 0.92 | 1.29 | 1.64 | 0.73 | 1.66 | 1.51 | 0.34 |
| $FeO_T$ | 1.66 | 1.35 | 1.56 | 1.53 | 1.53 | 1.64 | 1.55 | 1.51 | 1.66 | 1.18 |
| CaO | 33.99 | 35.55 | 34.54 | 36.60 | 35.73 | 34.57 | 36.85 | 34.97 | 34.19 | 36.62 |
| BaO | 1.54 | 1.53 | 1.33 | 1.70 | 0.82 | 1.28 | 1.02 | 1.29 | 1.51 | 1.19 |
| $Na_2O$ | 0.89 | 0.84 | 0.66 | 0.51 | 0.59 | 0.84 | 0.44 | 0.80 | 0.75 | 0.94 |
| Total | 98.45 | 99.48 | 99.20 | 98.28 | 99.14 | 98.02 | 100.66 | 100.19 | 99.54 | 99.00 |
| Structural formula based on 3 atoms of oxygens. | | | | | | | | | | |
| Na | 0.042 | 0.039 | 0.031 | 0.024 | 0.027 | 0.040 | 0.020 | 0.037 | 0.035 | 0.043 |
| Ca | 0.891 | 0.913 | 0.897 | 0.945 | 0.913 | 0.902 | 0.925 | 0.891 | 0.884 | 0.921 |
| Ba | 0.015 | 0.014 | 0.013 | 0.016 | 0.008 | 0.012 | 0.009 | 0.012 | 0.014 | 0.011 |
| La | 0.017 | 0.014 | 0.018 | 0.015 | 0.012 | 0.013 | 0.015 | 0.016 | 0.019 | 0.011 |
| Ce | 0.026 | 0.021 | 0.025 | 0.016 | 0.023 | 0.024 | 0.019 | 0.023 | 0.026 | 0.006 |
| Nd | 0.015 | 0.012 | 0.015 | 0.008 | 0.011 | 0.014 | 0.006 | 0.014 | 0.013 | 0.003 |
| Th | 0.006 | 0.004 | 0.005 | – | 0.002 | 0.003 | 0.002 | 0.003 | 0.004 | – |
| Total A | 1.011 | 1.018 | 1.004 | 1.023 | 0.996 | 1.009 | 0.996 | 0.995 | 0.996 | 0.994 |
| Ti | 0.952 | 0.961 | 0.952 | 0.956 | 0.966 | 0.958 | 0.964 | 0.974 | 0.967 | 0.981 |
| Fe | 0.034 | 0.027 | 0.032 | 0.031 | 0.031 | 0.033 | 0.030 | 0.030 | 0.033 | 0.023 |
| Al | 0.012 | 0.008 | 0.009 | 0.008 | 0.010 | 0.007 | 0.012 | – | – | – |
| Nb | 0.008 | 0.005 | 0.011 | 0.006 | 0.007 | 0.009 | 0.006 | 0.006 | 0.009 | 0.013 |
| Total B | 1.006 | 1.001 | 1.004 | 1.001 | 1.012 | 1.007 | 1.013 | 1.011 | 1.009 | 1.017 |

1-core, 2-1st zone, 3-2nd zone, 4-3rd zone; 5-core, 6-1st zone, 7-2nd zone; 8-core, 9-1st zone, 10-2nd zone

$FeO_T$ total Fe expressed as FeO

*n.d.* not detected (<0.15 wt.%)

(Figs. 7d and 8a). Hsu (1994) demonstrated the formation of cymrite by complete replacement of barite, which is also possible in P-12 given the significant quantity of barite present. Figure 8c shows barite being replaced at the margins in a manner similar to that illustrated by Hsu (1994) for cymrites from Nevada. In many areas, cymrite is altered to a hydrogrossular-like material (Fig. 8a, b, c; Table 10). This is the first report of cymrite from a lamproite.

## Apatite

Apatite occurs primarily as a late stage anhedral groundmass phase. Apatite crystals are also poikilitically-enclosed by groundmass phlogopite and richterite. Very small (<5 μm) sheaf-like and skeletal apatites are commonly observed in the groundmass and carbonate clasts. The skeletal apatites commonly enclose chloritic and carbonate material (Fig. 8d). Apatites are also closely associated with carbonate clasts and late stage calcite.

Representative compositions of apatites are given in Table 11. They are rich in BaO (up to 1.5 wt.%) and SrO (up to 3.2 wt.%), and contain considerable amounts of fluorine (up to 3.2 wt.%). They can be classified as fluor-apatites, and are similar to those reported in many lamproites by (Scott Smith and Skinner 1984; Thy et al. 1987; Edgar 1989; Mitchell and Bergman 1991). The BaO contents are comparable to apatites in West Kimberley lamproites. (Edgar 1989; Mitchell and Bergman 1991). The sheaf-like quench apatites are too small for quantitative analysis (Fig. 8d), although it is apparent that they are enriched in Sr and Ba.

## Calcite, barite, witherite, strontianite

Calcite occurs principally as anhedral patches throughout the groundmass and also as anhedral crystals up to 100 μm in size with distinct compositional zonation (Fig. 9a, b). The calcites are late stage residual material which incorporated in solid

**Table 7** Representative compositions (wt. %) of spinels in the groundmass

| | 1 | 2 | 3 | 4 | 5 | 6 | 7 | 8 | 9 | 10 |
|---|---|---|---|---|---|---|---|---|---|---|
| $TiO_2$ | 9.85 | 10.13 | 9.23 | 9.22 | 8.96 | 9.99 | 9.17 | 7.10 | 10.47 | 10.24 |
| $Al_2O_3$ | 0.42 | 0.65 | 0.31 | 0.29 | 0.00 | 4.73 | 0.47 | 0.97 | 1.35 | 0.63 |
| $Cr_2O_3$ | 0.51 | 0.48 | n.d. | 0.39 | 0.59 | n.d. | 0.49 | 12.49 | 3.28 | 2.66 |
| $FeO_T$ | 82.79 | 82.42 | 82.77 | 82.73 | 84.01 | 78.26 | 82.14 | 70.19 | 75.46 | 77.21 |
| MnO | 1.90 | 2.27 | 2.13 | 1.98 | 2.08 | 2.09 | 1.40 | n.d. | 1.36 | 0.55 |
| MgO | 1.30 | 0.47 | 1.53 | 1.41 | 0.71 | 0.53 | 1.39 | 4.98 | 3.25 | 4.75 |
| Total | 96.77 | 96.42 | 95.97 | 96.02 | 96.35 | 95.60 | 95.06 | 95.73 | 95.17 | 96.04 |
| FeO | 36.94 | 37.99 | 35.55 | 35.88 | 36.69 | 38.25 | 36.16 | 30.39 | 34.60 | 33.14 |
| $Fe_2O_3$ | 50.95 | 49.38 | 52.48 | 52.06 | 52.59 | 44.47 | 51.10 | 44.24 | 45.41 | 48.98 |
| Total | 101.88 | 101.37 | 101.23 | 101.24 | 101.62 | 100.06 | 100.18 | 100.16 | 99.72 | 100.95 |
| Structural formula calculated on the basis of four atoms of oxygen | | | | | | | | | | |
| Ti | 0.274 | 0.285 | 0.258 | 0.258 | 0.252 | 0.278 | 0.259 | 0.194 | 0.291 | 0.279 |
| Al | 0.018 | 0.029 | 0.014 | 0.013 | 0.000 | 0.206 | 0.021 | 0.042 | 0.059 | 0.027 |
| Cr | 0.015 | 0.014 | – | 0.011 | 0.017 | – | 0.015 | 0.359 | 0.096 | 0.076 |
| $Fe^{2+}$ | 1.143 | 1.187 | 1.106 | 1.118 | 1.147 | 1.183 | 1.137 | 0.924 | 1.070 | 1.006 |
| $Fe^{3+}$ | 1.419 | 1.388 | 1.470 | 1.459 | 1.479 | 1.238 | 1.446 | 1.211 | 1.263 | 1.338 |
| Mn | 0.060 | 0.072 | 0.067 | 0.062 | 0.066 | 0.065 | 0.045 | – | 0.043 | 0.017 |
| Mg | 0.072 | 0.026 | 0.085 | 0.078 | 0.040 | 0.029 | 0.078 | 0.270 | 0.179 | 0.257 |
| | 3.000 | 3.000 | 3.000 | 3.000 | 3.000 | 3.000 | 3.000 | 3.000 | 3.000 | 3.000 |

$FeO_T$ total Fe expressed as FeO

$Fe_2O_3$ and FeO calculated on a stoichiometric basis

*n.d.* not detected (<0.15 wt.%)

**Table 8** Representative compositions (wt. %) of atoll spinels

| | 1C | 1R | 2C | 2R | 3C | 3R | 4C | 4R | 5C | 5R | 6C | 6R |
|---|---|---|---|---|---|---|---|---|---|---|---|---|
| $TiO_2$ | 2.35 | 10.92 | 5.07 | 10.36 | 5.43 | 9.91 | 11.49 | 10.49 | 9.67 | 9.99 | 6.55 | 9.90 |
| $Al_2O_3$ | 6.85 | 0.48 | 7.82 | 0.75 | 7.54 | 0.87 | 4.08 | 0.78 | 3.66 | 0.53 | 6.35 | 0.46 |
| $Cr_2O_3$ | 53.03 | 0.35 | 44.28 | 1.33 | 42.20 | 2.16 | 11.88 | 0.50 | 15.12 | 0.39 | 37.30 | 0.50 |
| $FeO_T$ | 28.59 | 81.82 | 30.94 | 79.24 | 33.34 | 76.84 | 62.62 | 82.34 | 61.28 | 81.72 | 37.65 | 81.51 |
| MnO | 0.89 | 2.38 | 0.92 | 2.11 | 0.72 | 1.90 | 0.92 | 1.99 | 0.70 | 1.68 | 0.75 | 1.64 |
| MgO | 8.46 | 1.05 | 9.43 | 1.26 | 8.79 | 3.52 | 7.48 | n.d. | 6.78 | 0.61 | 9.01 | 0.38 |
| Total | 100.17 | 97.00 | 98.46 | 95.05 | 98.02 | 95.20 | 98.47 | 96.10 | 97.21 | 94.92 | 97.61 | 94.39 |
| FeO | 21.62 | 37.85 | 22.19 | 36.69 | 23.53 | 33.12 | 30.80 | 39.21 | 29.98 | 37.73 | 23.93 | 37.86 |
| $Fe_2O_3$ | 7.74 | 48.86 | 9.72 | 47.29 | 10.90 | 48.58 | 35.36 | 47.93 | 34.79 | 48.88 | 15.25 | 48.51 |
| Total | 100.95 | 101.90 | 99.43 | 99.79 | 99.11 | 100.07 | 102.01 | 100.90 | 100.70 | 99.82 | 99.14 | 99.25 |
| Structural formula calculated on the basis of four atoms of oxygen | | | | | | | | | | | | |
| Ti | 0.060 | 0.304 | 0.129 | 0.293 | 0.139 | 0.275 | 0.297 | 0.297 | 0.255 | 0.285 | 0.169 | 0.285 |
| Al | 0.272 | 0.021 | 0.312 | 0.033 | 0.303 | 0.038 | 0.166 | 0.035 | 0.151 | 0.024 | 0.257 | 0.021 |
| Cr | 1.413 | 0.010 | 1.183 | 0.040 | 1.138 | 0.063 | 0.323 | 0.015 | 0.420 | 0.012 | 1.012 | 0.015 |
| $Fe^{2+}$ | 0.609 | 1.172 | 0.627 | 1.156 | 0.672 | 1.022 | 0.887 | 1.234 | 0.880 | 1.197 | 0.687 | 1.210 |
| $Fe^{3+}$ | 0.196 | 1.361 | 0.247 | 1.340 | 0.280 | 1.349 | 0.916 | 1.357 | 0.919 | 1.395 | 0.394 | 1.395 |
| Mn | 0.025 | 0.075 | 0.026 | 0.067 | 0.021 | 0.059 | 0.027 | 0.063 | 0.021 | 0.054 | 0.022 | 0.053 |
| Mg | 0.425 | 0.058 | 0.475 | 0.071 | 0.447 | 0.194 | 0.384 | – | 0.355 | 0.034 | 0.461 | 0.022 |
| | 3.000 | 3.000 | 3.000 | 3.000 | 3.000 | 3.000 | 3.000 | 3.000 | 3.000 | 3.000 | 3.000 | 3.000 |

$FeO_T$ total Fe expressed as FeO

$Fe_2O_3$ and FeO calculated on a stoichiometric basis

*C* core, *R* rim, *n.d.* not detected (<0.15 wt.%)

**Table 9** Representative compositions (wt. %) of gittinsite and strontium zirconium silicate

| | 1 | 2 | 3 | 4 | 5 | 6 | 7 | 8 | 9 | 10 | 11 |
|---|---|---|---|---|---|---|---|---|---|---|---|
| $SiO_2$ | 38.90 | 39.00 | 38.76 | 38.37 | 39.70 | 40.23 | 36.41 | 36.89 | 37.82 | 38.41 | 37.21 |
| Na2O | n.d. | n.d. | n.d. | n.d. | n.d. | n.d. | 2.13 | 2.75 | 2.96 | 4.22 | 3.09 |
| CaO | 17.41 | 17.39 | 17.77 | 17.53 | 17.22 | 16.93 | 1.06 | 4.9 | 4.75 | 4.52 | 2.09 |
| $FeO_T$ | 1.37 | 1.21 | 1.18 | 1.09 | 1.25 | 1.74 | n.d. | n.d. | n.d. | n.d. | n.d. |
| $ZrO_2$ | 39.33 | 39.25 | 38.82 | 38.62 | 39.87 | 36.86 | 35.24 | 38.69 | 38.31 | 37.38 | 36.32 |
| BaO | 1.65 | 1.56 | 1.16 | 1.52 | 1.44 | 1.23 | 1.98 | 2.03 | 1.78 | n.d. | 1.87 |
| $HfO_2$ | 1.22 | 1.00 | 0.85 | 1.12 | 0.89 | 1.08 | n.d. | 1.64 | 1.4 | 1.27 | n.d. |
| MgO | 1.82 | 1.29 | 1.38 | 0.94 | 1.53 | 2.82 | 1.44 | n.d. | n.d. | n.d. | n.d. |
| SrO | n.d. | n.d. | n.d. | n.d. | n.d. | n.d. | 22.83 | 14.42 | 14.22 | 14.52 | 20.46 |
| Total | 101.70 | 100.70 | 99.92 | 99.19 | 101.90 | 100.89 | 101.09 | 101.32 | 101.24 | 100.32 | 101.04 |
| Structural formula based on 7 atoms of oxygen | | | | | | | | | | | |
| Si | 1.945 | 1.964 | 1.960 | 1.964 | 1.969 | 1.993 | 2.014 | 1.994 | 2.026 | 2.047 | 2.040 |
| Na | 0.000 | 0.000 | 0.000 | 0.000 | 0.000 | 0.000 | 0.228 | 0.288 | 0.307 | 0.436 | 0.328 |
| Ca | 0.933 | 0.938 | 0.963 | 0.962 | 0.915 | 0.899 | 0.063 | 0.284 | 0.273 | 0.258 | 0.123 |
| Fe | 0.057 | 0.051 | 0.050 | 0.047 | 0.052 | 0.072 | 0.000 | 0.000 | 0.000 | 0.000 | 0.000 |
| Zr | 0.959 | 0.964 | 0.957 | 0.964 | 0.964 | 0.890 | 0.951 | 1.020 | 1.000 | 0.971 | 0.971 |
| Ba | 0.032 | 0.031 | 0.023 | 0.030 | 0.028 | 0.024 | 0.043 | 0.043 | 0.037 | 0.000 | 0.040 |
| Hf | 0.017 | 0.014 | 0.012 | 0.016 | 0.013 | 0.015 | 0.000 | 0.025 | 0.021 | 0.019 | 0.000 |
| Mg | 0.136 | 0.097 | 0.104 | 0.072 | 0.113 | 0.208 | 0.119 | 0.000 | 0.000 | 0.000 | 0.000 |
| Sr | 0.000 | 0.000 | 0.000 | 0.000 | 0.000 | 0.000 | 0.732 | 0.452 | 0.442 | 0.449 | 0.650 |
| Total | 4.079 | 4.058 | 4.070 | 4.055 | 4.054 | 4.101 | 4.150 | 4.105 | 4.106 | 4.180 | 4.153 |

$FeO_T$ Total Fe expressed as FeO

1–6: Gittinsite; 7–11: Sr analog of gittinsite

*n.d.* not detected (<0.15 wt.%)

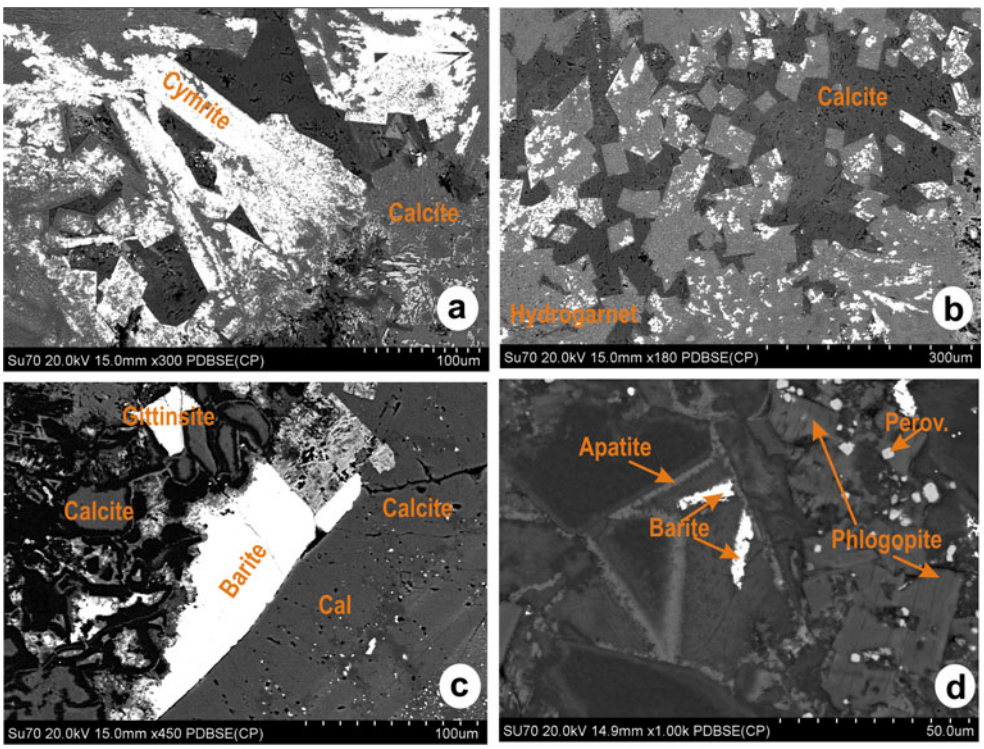


**Fig. 8** **a** Euhedral prismatic cymrite crystals and hydrogarnet in carbonate (BSE image). **b** Euhedral rectangular hydrogarnet relicts after cymrite (BSE image). **c** Prismatic barite replaced by cymrite and hydrogarnet material along the margins. Also seen are gittinsite and residual calcite (BSE image). **d** Skeletal apatites in the groundmass (BSE image)

**Table 10** Representative compositions (wt. %) of cymrite and hydrogarnets

| | 1 | 2 | 3 | 4 | 5 | 6 | 7 | 8 | 9 | 10 | 11 |
|---|---|---|---|---|---|---|---|---|---|---|---|
| $SiO_2$ | 32.27 | 32.07 | 32.16 | 32.40 | 32.89 | 32.99 | 32.93 | 36.85 | 36.08 | 33.63 | 34.72 |
| $Al_2O_3$ | 25.79 | 27.51 | 26.77 | 27.06 | 26.73 | 27.08 | 26.36 | 15.28 | 14.67 | 18.73 | 18.97 |
| $FeO_T$ | n.d. | n.d. | n.d. | n.d. | n.d. | n.d. | n.d. | 4.44 | 3.99 | 4.11 | 4.38 |
| CaO | 2.34 | 0.76 | 0.67 | 0.72 | 1.11 | 0.51 | 0.88 | 38.05 | 38.96 | 38.31 | 38.61 |
| $K_2O$ | 0.49 | n.d. | n.d. | n.d. | 0.43 | 0.50 | 0.58 | n.d. | n.d. | n.d. | n.d. |
| BaO | 37.57 | 38.79 | 38.97 | 38.20 | 37.98 | 37.82 | 37.34 | n.d. | n.d. | n.d. | n.d. |
| Total | 98.46 | 99.13 | 98.57 | 98.38 | 99.14 | 98.9 | 98.09 | 94.62 | 93.70 | 94.78 | 96.68 |
| Structural formulae calculated on the basis of 8 atoms of oxygen | | | | | | | | | | | |
| Si | 2.022 | 1.992 | 2.016 | 2.019 | 2.034 | 2.037 | 2.052 | | | | |
| Al | 1.905 | 2.014 | 1.978 | 1.987 | 1.948 | 1.971 | 1.936 | | | | |
| Ca | 0.157 | 0.051 | 0.045 | 0.048 | 0.074 | 0.034 | 0.059 | | | | |
| K | 0.039 | – | – | – | 0.034 | 0.039 | 0.046 | | | | |
| Ba | 0.922 | 0.944 | 0.957 | 0.933 | 0.920 | 0.915 | 0.912 | | | | |
| Total | 5.05 | 5.00 | 5.00 | 4.99 | 5.01 | 5.00 | 5.00 | | | | |

1–7: cymrite; 8–11:hydrogarnets

$FeO_T$ total Fe expressed as FeO

*n.d.* not detected (<0.15 wt.%)

solution up to 8 wt.% BaO and 2 wt.% SrO from late-stage deuteric fluids. Late-stage calcite veins are also common. Calcite is intimately intergrown with witherite and barite. Barites are subhedral-to-anhedral in habit and vary in size from <10 μm to up to 300 μm (Fig. 8c, d). Barite commonly occurs in the carbonate clasts together with witherite, strontianite, and Ba-Sr-bearing calcite. The strontianite is present as small round inclusions (<20 μm) within pyroxene phenocrysts (Fig. 4a), in the groundmass and carbonate clasts, and contains up to 0.4 wt.% $FeO_T$ and up to 1.4 wt.% BaO (Table 11). Representative compositions of calcite, barite, witherite and strontianite are given in Table 11.

## Hydrogarnet, chlorite and serpentine

Hydrogarnet, chlorite, and serpentine are common alteration products of olivine, pyroxene, phlogopite, and celsian-cymrite. The chlorite and serpentine commonly occur at the rims and margins of altered olivine and pyroxene crystals. Chlorite and hydrogarnet are observed to form after pyroxenes in poikilitic phlogopite. Poikilitic richterite and pyroxene also are altered to hydrogarnets by deuteric fluids (Fig. 4c). Cymrite crystals, in many instances, are completely pseudomorphed by hydrogarnet-like material (Fig. 8b; Table 10).

**Table 11** Representative compositions (wt. %) of apatite, calcite, barite, witherite, strontianite

| | 1 | 2 | 3 | 4 | 5 | 6 | 7 | 8 | 9 | 10 | 11 | 12 | 13 | 14 | 15 | 16 |
|---|---|---|---|---|---|---|---|---|---|---|---|---|---|---|---|---|
| $P_2O_5$ | 38.74 | 38.78 | 37.44 | 33.05 | 34.17 | n.d. | n.d. | n.d. | n.d. | n.d. | n.d. | n.d. | n.d. | n.d. | n.d. | n.d. |
| $SiO_2$ | 0.84 | 1.28 | 1.62 | n.d. | 0.98 | n.d. | n.d. | n.d. | n.d. | n.d. | n.d. | n.d. | n.d. | n.d. | n.d. | n.d. |
| $FeO_T$ | n.d. | 0.37 | 0.45 | 0.53 | 0.31 | n.d. | n.d. | n.d. | n.d. | n.d. | n.d. | n.d. | n.d. | 0.28 | 0.42 | n.d. |
| MgO | n.d. | n.d. | n.d. | n.d. | n.d. | n.d. | n.d. | n.d. | n.d. | n.d. | n.d. | 0.48 | n.d. | n.d. | n.d. | 0.45 |
| CaO | 53.96 | 53.68 | 53.29 | 49.40 | 48.82 | 52.80 | 48.88 | 47.65 | 0.34 | 0.70 | 19.83 | 19.31 | 20.85 | 14.97 | 13.57 | 18.40 |
| SrO | 2.32 | 2.52 | 2.41 | 2.16 | 3.15 | 0.89 | 1.98 | 1.72 | n.d. | n.d. | n.d. | 0.86 | 0.82 | 45.01 | 46.19 | 41.90 |
| BaO | n.d. | n.d. | n.d. | 1.45 | 0.64 | 3.08 | 4.96 | 7.24 | 62.58 | 62.47 | 45.51 | 45.78 | 42.08 | 1.39 | 1.38 | 1.43 |
| $Na_2O$ | n.d. | n.d. | 0.31 | 2.09 | 1.62 | n.d. | n.d. | n.d. | n.d. | n.d. | n.d. | n.d. | n.d. | n.d. | n.d. | n.d. |
| $SO_3$ | n.d. | n.d. | n.d. | n.d. | n.d. | n.d. | n.d. | n.d. | 35.36 | 34.59 | n.d. | n.d. | n.d. | n.d. | n.d. | n.d. |
| F | 3.56 | 3.21 | 2.78 | 3.20 | 2.09 | n.d. | n.d. | n.d. | n.d. | n.d. | n.d. | n.d. | n.d. | n.d. | n.d. | n.d. |
| Total | 97.92 | 98.49 | 97.13 | 90.53 | 90.90 | 56.77 | 55.82 | 56.61 | 98.28 | 97.76 | 65.34 | 66.43 | 63.75 | 61.65 | 61.56 | 62.18 |

1–5:-apatite; 6–8: calcite; 9–10:barite; 11–13: witherite; 14–16: strontianite

$FeO_T$ total Fe expressed as FeO

*n.d.* not detected (<0.15 wt.%)

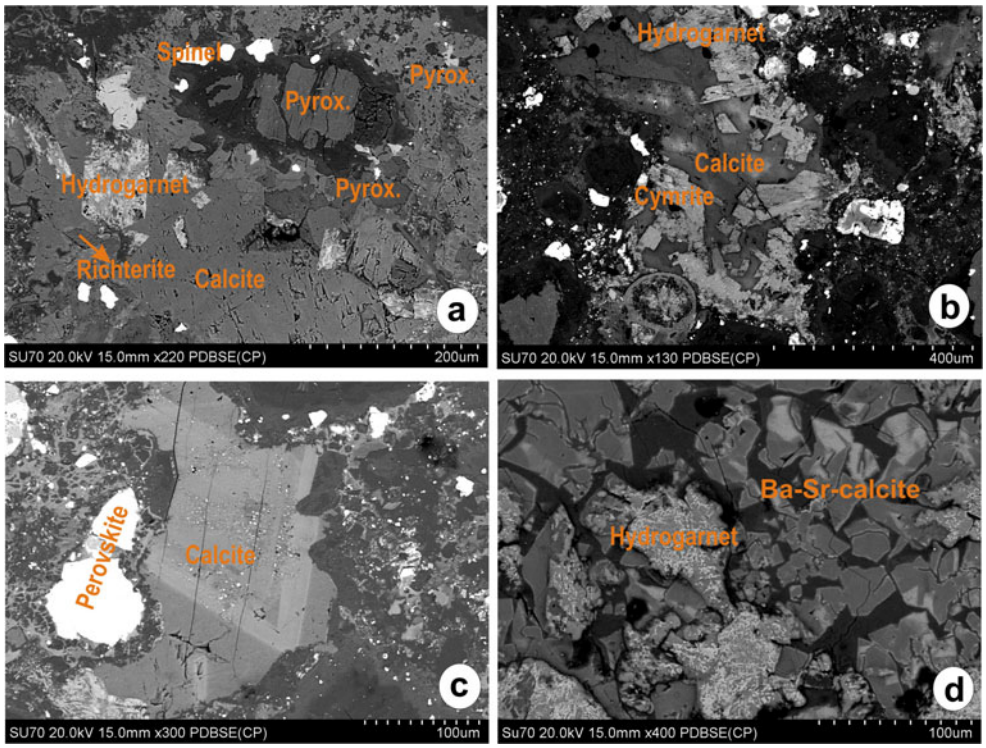


**Fig. 9** **a** Contact of groundmass material and carbonate clast with reaction pyroxenes. Also seen are microphenocryst and groundmass pyroxenes (BSE image). **b** Groundmass cymrite and hydrogranet (BSE image). **c** Residual late stage groundmass calcite (BSE image). **d** Late stage barium-strontium enriched groundmass calcite and hydrogarnet (BSE image)

## Discussion

### Classification

This study demonstrates that in terms of a mineralogical-genetic classification the P-12 intrusion is a *bona fide* lamproite and ***not*** an archetypal kimberlite. This conclusion is based on the presence and compositions of: phenocrystal forsteritic olivine; Al-Na-poor diopside; Fe-Ti-rich, Ba-Al-poor phlogopite-tetraferriphlogopite; K-Ti-richterite; and Mg-poor spinel. Accessory minerals include relatively-REE-poor perovskite and apatite together with late-stage deuteric

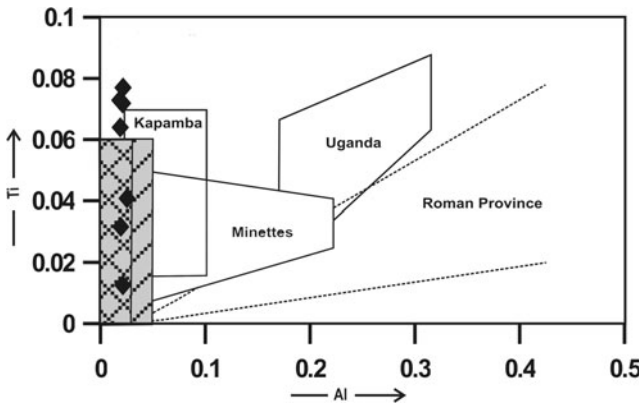


**Fig. 10** Compositional variation (Ti vs. Al) of pyroxenes from P-12 lamproite. Compositional fields and trends for lamproites and orangeites (*grey* field), minettes, Roman province lavas and kamafugites from Mitchell and Bergman (1991)

barite, Ba-Sr-bearing calcite, witherite and strontianite. Secondary phases include cymrite and hydrogarnet after celsian. Gittinsite and its Sr-analog ($SrZrSi_2O_7$) are recognized for the first time in a lamproite. The low alumina contents of the P-12 phlogopites, pyroxenes, amphiboles, spinels, and the occurrence of gittinsite indicate the peralkaline nature of the P-12 parental magma.

P-12 contains up to 25 modal % olivine principally as phenocrysts and microphenocrysts. Macrocrystal olivines (Fig. 2a) are rare, in common with the Wajrakarur P2-West lamproite and many other olivine lamproites (Scott Smith and Skinner 1984; Mitchell and Bergman 1991; Gurmeet Kaur and Mitchell 2013), in contrast to their common occurrence kimberlites (Mitchell 1986, 1995). Pyroxenes belong to five paragenetic types and exhibit only subtle differences in terms of their $Na_2O$, CaO, FeO and $TiO_2$ contents (Table 2). All P-12 clinopyroxenes occupy the lamproite field in a Ti vs. Al diagram (Fig. 10) (Mitchell and Bergman 1991). The acicular pyroxene forming after olivine and the euhedral-to-subhedral pyroxenes in the carbonate clasts with hydrogarnet rims are unique to P-12 and have not been described previously from lamproites (Figs. 11, 12, 13, 14, and 15).

All phlogopites in P-12 are extremely poor in $Al_2O_3$ (<5 wt.%). and are sodic titanian tetraferriphlogopites, characteristic of lamproites (Mitchell and Bergman 1991). The amphiboles are titanian potassium richterites and titanian potassium magnesio-katophorites and similar to amphiboles from the West Kimberley and Smoky Butte

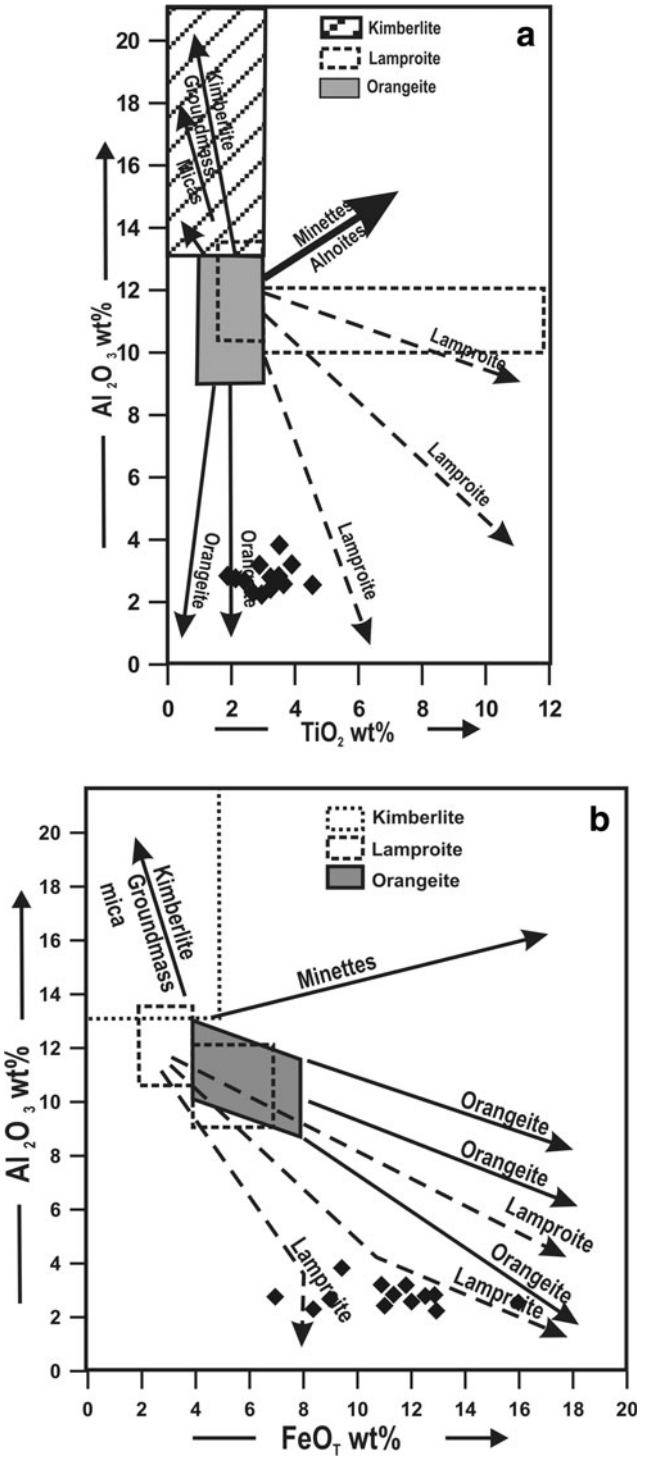


**Fig. 11** **a** $Al_2O_3$ vs. $TiO_2$ (wt.%) compositional variation of phlogopite in P-12. **b** $Al_2O_3$ vs. $FeO_T$ compositional variation of phlogopite in P-12. Compositional fields and trends for kimberlites, lamproite, orangeite and minette micas from Mitchell (1995)

lamproites (Mitchell and Bergman 1991). Note that such groundmass amphiboles are absent from kimberlites, but are an important groundmass phase in lamproites (Mitchell and Bergman 1991).

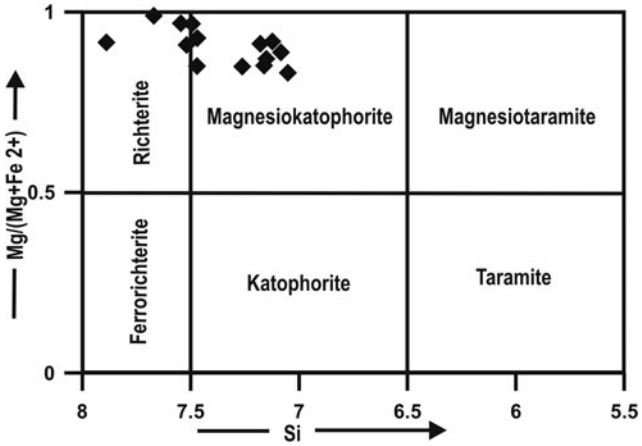


**Fig. 12** Mg/(Mg+Fe2$^{+}$) vs. Si (a.p.f.u) compositional variation of amphiboles in P-12 lamproite (after Leake et al. 1997)

Atoll spinels, which are common in kimberlites, are present in P-12. Similar atoll spinels have been described from the Wajrakarur P-5 and P-13 lamproites, by Gurmeet Kaur et al. (2013). The atoll spinels have titanian aluminous magnesiochromites cores with rims of magnesian titaniferous magnetite. The groundmass spinels, mostly ulvöspinels, are enriched in iron and titanium and low in alumina, (Mitchell and Bergman 1991). The atoll spinels and the groundmass spinels follow the compositional evolution trend of lamproite spinels (Mitchell and Bergman 1991), and hence are poor in

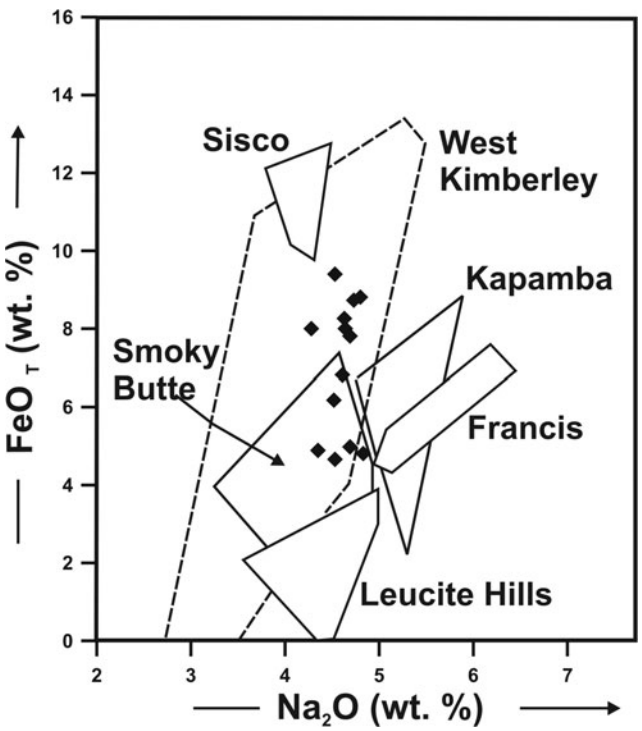


**Fig. 13** $FeO_T$ vs. $Na_2O$ compositional variation of amphiboles from P-12. Compositional fields and trends for amphiboles in lamproites from Mitchell and Bergman (1991)

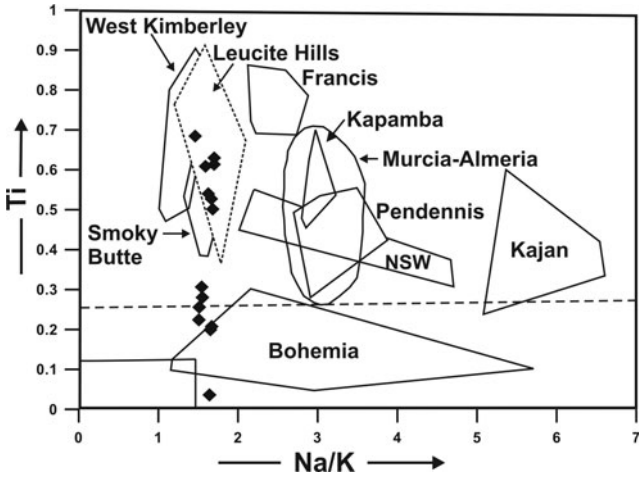


**Fig. 14** Ti vs. Na/K (a.p.f.u) compositional variation of amphiboles in P-12 lamproite. Compositional fields and trends for amphiboles in lamproites and other potassic rocks from Mitchell and Bergman (1991)

the qandilite end-member spinel characteristic of archetypal kimberlite.

Apatites in P-12 are rich in BaO (up to 1.5 wt.%), SrO (up to 3.2 wt.%) and fluorine (up to 3.2 wt.%) can be classified as fluor-apatites, and are similar to those occurring in lamproites (Scott Smith and Skinner 1984; Thy et al. 1987; Edgar 1989; Mitchell and Bergman 1991). Perovskite compositions are not diagnostic of magma-type and are essentially unevolved REE-bearing, Sr-poor $CaTiO_3$.

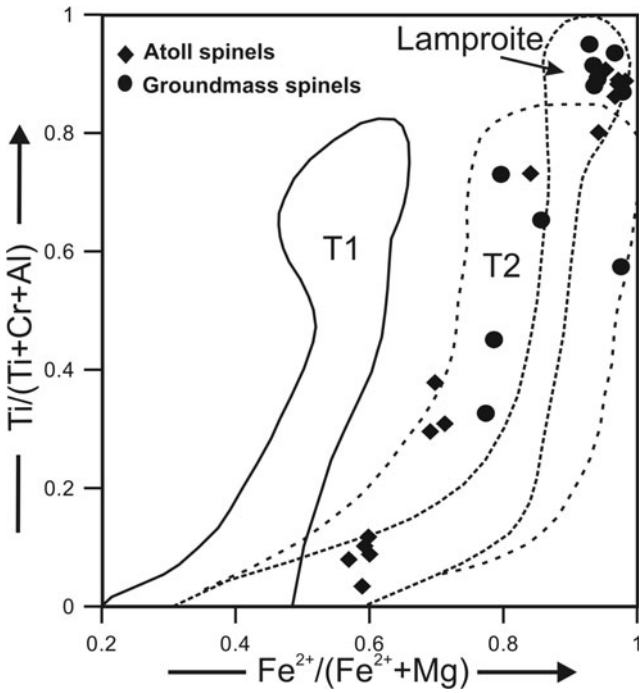


**Fig. 15** Compositional variation of spinels from P-12 projected onto the front face of the reduced iron spinel compositional prism (Mitchell 1986). Compositional fields and trends for spinels from kimberlites (T1) and lamproites (T2) from Mitchell (1986, 1995)

Although calcite is not common in lamproites, it occurs in P-12 as a minor late stage residual phase. The calcite is enriched in BaO (up to 8 wt.%) and SrO (up to 2 wt.%) and crystallized from the late-stage deuteric fluids. The calcite is intimately intergrown with witherite and barite. Strontianite is present as small round inclusions (<20 μm) within pyroxene phenocrysts, in the groundmass and carbonate clasts. Hydrogarnet, chlorite, and serpentine are common alteration products of olivine, pyroxene, phlogopite, and cymrite.

Three minerals, gittinsite, $SrZrSi_2O_7$, and cymrite are reported for the first time from a lamproite. Gittinsite and cymrite have been previously recognized from carbonatites (Ansell et al. 1980; Birkett et al. 1992; Chakhmouradian and Zaitsev 2002; Sorokhtina et al. 2008). Gittinsite and $SrZrSi_2O_7$ occur in P-12 in association with calcite, chlorite, pyroxene, and barite in the groundmass. Gittinsite has been recognized in peralkaline granites and syenites in the Kipawa and Strange Lake complexes and from carbonatites at Afrikanda (Ansell et al. 1980; Birkett et al. 1992; Chakhmouradian and Zaitsev 2002). The groundmass and the carbonate clasts host prismatic cymrite crystals which are interpreted to be pseudomorphs after potassium feldspar-celsian and/or barite (Essene 1967; Hsu 1994; Moro et al. 2001). Cymrites in association with carbonates have been reported only from the Kovdor carbonatite (Sorokhtina et al. 2008). Cymrite crystals are commonly completely pseudomorphed by hydrogarnet-like material. Priderite, wadeite, and titanosilicates, such as shcherbakovite or barytolamprophyllite, are not present in P-12.

The origin of the carbonate clasts remains enigmatic. Their texture and mineralogy suggests that pre-existing carbonate has reacted with the lamproite host resulting in the metasomatic development of cymrite and hydrogarnet together with reaction mantles of acicular diopside. It cannot be determined whether-or-not these clasts are xenoliths of sedimentary carbonate analogous to those described by Chalapathi Rao et al. (2010) from the Siddanpalli intrusion.

The above textural and mineralogical data demonstrate that the P-12 hypabysal intrusion is a *bonafide* richterite diopside olivine lamproite in contrast to previous studies which have described the intrusion as a kimberlite (Neelkantam 2001; Ravi et al. 2009; Fareeduddin and Mitchell 2012; Chalapathi Rao et al. 2013). The magma from which P-12 was formed is best regarded as a local manifestation of a particular variety of cratonic potassic magmatism. Similar conclusions have been made for the Wajrakurur P2-West, P-5, P-13, P-3 and P-4 intrusions (Mitchell 2006; Gurmeet Kaur et al. 2012a, b, 2013; Gurmeet Kaur and Mitchell 2013). As it is now evident that the Wajrakurur field contains *bona fide* lamproites it is reasonable to conclude that many of the "para-kimberlites" in this field, which have not been subjected to detailed mineralogical-genetic classification, are also lamproites and *not* kimberlites.

## Geodynamic considerations

Although the genesis of the P-12, and other lamproites, in eastern India is not the focus of this paper some comments on the geodynamic and petrogenetic implications of our conclusions are warranted. Figure 16 shows that all of the lamproite fields along the eastern margin of India lie in a belt approximately parallel to the line of deformed alkaline rock complexes defined by Leelanandum et al. (2006) and Burke and Khan (2006) in the Eastern Ghats Mobile Belt and Southern Granulite Terrain. We consider this disposition unlikely to be merely a geographic coincidence and to have petrological and geodynamic significance.

Leelanandum et al. (2006) consider that convergent plate margin processes leading to the development of Eastern Ghats Mobile Belt appear to have begun 1.8 Ga ago, and that convergent plate boundary phenomena have left peaks in isotopic records at 1 Ga and c. 750 Ma. The 1 Ga event coincides with the emplacement of the eastern Indian lamproites and also of those in the Bundelkhand craton (see summmary of ages in Fareeduddin and Mitchell 2012).

Das Sharma and Ramesh (2013) have interpreted data obtained primarily from passive seismological studies of southeast India, together with constraints from several other geophysical geological, and geochronological studies, to indicate the preservation in the subcontinental lithospheric mantle of relict subducted oceanic slab material at depths of 160–220 km. The origins of this material are related to suturing of the Eastern Dharwar craton and Eastern Ghats mobile belt possibly during the Mesoproterozoic (ca. 1.6 Ga). Das Sharma and Ramesh (2013) suggest that a thick lithospheric root underlies southeast India, with the Archean Eastern Dharwar craton and the Proterozoic Eastern Ghats mobile belt being underlain by a relict subducted slab within the upper mantle. The depth (160–220 km) of this feature also coincides with the diamond stability field. Clearly such subducted material, if metasomatized, could provide a source for lamproitic magmatism, and it is important to note that several geochemical studies of eastern Indian para-kimberlites and lamproites have suggested a role for subducted components in their genesis, together with formation in the subcontinental lithospheric mantle, rather than convecting asthenospheric mantle (Chalapathi Rao and Dongre 2009; Chalapathi Rao et al. 2010).

The extensive near-linear disposition of the east Indian para-kimberlites and lamproites is not in accord with the

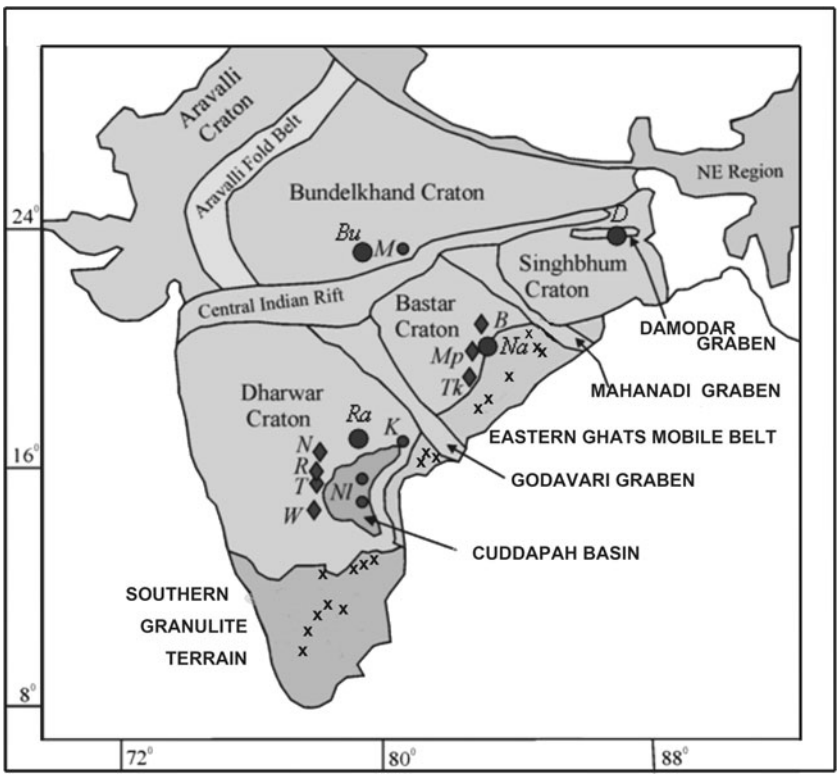


**Fig. 16** Distribution of kimberlites and lamproites in the Bundelkhand, Singhbhum, Bastar, and Dharwar cratons of the Indian subcontinent. Diamonds (◊), circles (o) and crosses (x) in the figure refer to the locations of kimberlites, lamproites and deformed alkaline rocks and carbonatites (DARC), respectively. *Bu* Bunder lamproites, *M* Majhgawan lamproite field, *B* Basna kimberlite field, *Na* Nawapara lamproite field, *Mp* Mainpur kimberlite field, *Tk* Tokapal kimberlite field, *Ra* Ramadugu lamproite field, *N* Narayanpet kimberlite field, *R* Raichur kimberlite field, *T* Tungabhadra kimberlite field, *W* Wajrakarur kimberlite field, *Nl* Nallamalai lamproite field, *K* Krishna lamproite field, and *D* Damodar valley lamproites (modified after Leelanandum et al. 2006; Burke and Khan 2006; Das Sharma and Ramesh 2013)

ascent of a mantle plume causing partial melting of the sources. Partial melting is more probably related to decompressional melting resulting from uplift and extensional tectonics, as intially suggested by Chalapathi Rao et al. (2004). Uplift over a wide area can also account for the contemporaneous emplacement of the Mahjgawan lamproite from subducted sources below the Bundelkhand craton.

## Conclusions

The Wajrakurur P-12 hypabyssal intrusion is classified on a mineralogical-genetic basis as a richterite diopside olivine lamproite and not a *bona-fide* kimberlite. This intrusion and other lamproites in eastern India were emplaced at c. 1 Ga as a result of extensional decompressional melting of metasomatized subducted material underlying several Archean cratons.

**Acknowledgments** This work was supported by the Natural Sciences and Engineering Research Council of Canada, Almaz Petrology, and Lakehead University. Staff of the Geological Survey of India in Bangalore and Wajrakarur are thanked for assistance in the field. Gurmeet Kaur wishes to acknowledge Panjab University, Chandigarh, India for granting leave to pursue research on Indian lamproites at Lakehead University. Valerie Dennison is thanked for pre-production copy editing of the text.

## References

Ansell HG, Roberts AC, Platt AG, Sturman BD (1980) Gittinsite, a new calcium zirconium silicate from the Kipawa agpaitic syenite complex, Quebec. Can Mineral 18:201–203

Birkett TC, Miller RR, Roberts AC, Mariano AN (1992) Zirconium-bearing minerals of the Strange Lake intrusive complex, Quebec-Labrador. Can Mineral 30:191–205

Burke K, Khan S (2006) Geoinformatic approach to global nepheline syenite and carbonatite distribution: testing a Wilson cycle model. Geosphere 2:53–60

Chakhmouradian AR, Zaitsev AN (2002) Calcite-amphibole-clinopyroxene rock from the Afrikanda complex, Kola Peninsula, Russia: mineralogy and a possible link to carbonatites: III. Silicate minerals. Can Mineral 40:1347–1374

Chalapathi Rao NV, Dongre AD (2009) Mineralogy and geochemistry of kimberlites NK-2 and KK-6 Narayanpet kimberlite field, eastern Dharwar Craton, southern India: evidence for a transitional kimberlite signature. Can Mineral 47:1117–1135

Chalapathi Rao NV, Gibson SA, Pyle DM, Dickin AP (2004) Petrogenesis of Proterozoic lamproites and kimberlites from the Cuddapah basin and Dharwar craton, Southern India. J Petrol 45: 907–948

Chalapathi Rao NV, Dongre AN, Kamde G, Srivastava RK, Sridhar M, Kaminsky FE (2010) Petrology, geochemistry and genesis of newly discovered Mesoproterozoic highly magnesian, calcite-rich kimberlites from Siddanpalli, eastern Dharwar craton, southern India: products of subduction-related magmatic sources? Mineral Petrol 161: 721–742

Chalapathi Rao NV, Creaser RA, Lehmann B, Panwar BK (2013) Re-Os isotope study of Indian kimberlites and lamproites: implications for mantle source and cratonic evolution. Chem Geol 353:36–47

Das Sharma S, Ramesh DS (2013) Imaging mantle lithosphere for diamond prospecting in southeast India. Lithosphere 5:331–342

Edgar AD (1989) Barium- and strontium-enriched apatites in lamproites from West Kimberley, Western Australia. Am Mineral 74:889–895

Essene EJ (1967) An occurrence of cymrite in the Franciscan formation, California. Am Mineral 52:1887–1890

Fareeduddin, Mitchell RH (2012) Diamonds and their source rocks in India. Geol Soc India, Bangalore. 434pp

Foley SF, Taylor WR, Green DH (1986) The role of fluorine and oxygen fugacity in the genesis of the ultrapoatssic rocks. Contrib Mineral Petrol 94:183–192

Fritschle T, Prelević D, Foley SF, Jacob DE (2013) Petrological characterization of the mantle source of Mediterranean lamproites: Indications from major and trace elements of phlogopite. Chem Geol 353:267–279

Gurmeet Kaur, Mitchell RH (2013) Mineralogy of the P2-West "Kimberlite", Wajrakarur kimberlite field, Andhra Pradesh, India: kimberlite or lamproite? Mineral Mag 77:3175–3196

Gurmeet Kaur, Korakoppa M, Fareeduddin (2012a) Petrology of P-5 and P-13 kimberlite from Lattavaram kimberlite cluster, Wajrakarur Kimberlite Field, Andhra Pradesh, India. 10th International Kimberlite Conference, 6th to 11th February, 2012, Bangalore, India, Extended Abstract

Gurmeet Kaur, Pruseth KL, Fareeduddin, Korakoppa M (2012b) Are Wajrakarur kimberlites from Andhra Pradesh, India, true kimberlites? 34th International Geological Congress, 5th to 10th August, 2012, Brisbane, Australia, Abstract

Gurmeet Kaur, Korakoppa M, Fareeduddin, Pruseth KL (2013) Petrology of P-5 and P-13 "kimberlites" from Lattavaram kimberlite cluster, Wajrakarur Kimberlite Field, Andhra Pradesh, India: Reclassification as lamproites. Proceedings of the 10th International Kimberlite Conference 1: 183–194

Hogarth D (1997) Mineralogy of leucite-bearing dykes from Napoleon Bay, Baffin Island; multistage Proterozoic lamproites. Can Mineral 35:53–78

Hsu LC (1994) Cymrite: new occurrence and stability. Contrib Mineral Petrol 118:314–320

Huntelaar ME, Cordfunke EHP, Van Vlaanderen P, Ijdo DJW (1994) $SrZrSi_2O_7$. Acta Crystallogr C50:988–991

Jacobsen UK (1990) A hydrated barium silicate in unmetamorphosed sedimentary rocks of central North Greenland. Mineral Mag 54(81):89

Jaques AL, Lewis JD, Smith CB (1986) The kimberlites and lamproites of western Australia. Geol Surv W Aust Bull 132–268

Kuehner SM (1980) Petrogenesis of ultrapotassic rocks, Leucite Hills, Wyoming. M.Sc thesis, Univ Western Ontario, London, Ontario

Kuehner SM, Edgar AD, Arima M (1981) Petrogenesis of the ultrapotassic rocks from the Leucite hills, Wyoming. Am Mineral 66:663–677

Leake BE, Woolley AR, Arps CES, Birch WD, Gilbert MC, Grice JD, Hawthorne FC, Kato A, Kisch HJ, Krivovichev VG, Linthout K, Laird J, Mandarino JA, Maresch WV, Nickel EH, Rock NMS, Schumacher JC, Smith DC, Stephenson NCN, Ungaretti L, Whittaker EJW, Guo Y (1997) Nomenclature of amphiboles: report of the subcommittee on amphiboles of the International Mineralogical Association, Commission on New Minerals and Mineral Names. Can Mineral 35:219–246

Leelanandum C, Burke K, Ashwal LD, Webb SJ (2006) Proterozoic mountain building in Peninsular India: an analysis based primarily on alkaline rock distribution. Geol Mag 143:195–212

Liferovich RP, Mitchell RH (2005) Composition and paragenesis of Na-, Nb-, and Zr-bearing titanite from Khibina, Russia, and crystal structure data for synthetic analogues. Can Mineral 43:795–812

Mitchell RH (1981) Titaniferrous phlogopites from the Leucite lamproites of the West Kimberley area, Western Australia. Contrib Mineral Petrol 76:243–251

Mitchell RH (1986) Kimberlites: mineralogy, geochemistry and petrology. Plenum Press, New York, **442pp**

Mitchell RH (1989) Compositional variation of micas from the Leucite hills lamproites. 28th International Geological Congress. Washington, Extended abstract 2, pp 446–447

Mitchell RH (1995) Kimberlites, orangeites, and related rocks. Plenum Press, New York, **410pp**

Mitchell RH (2002) Perovskites: modern and ancient. Almaz Press Inc., Thunder Bay, **319pp**

Mitchell RH (2006) Potassic magmas derived from metasomatized lithospheric mantle: nomenclature and relevance to exploration for diamond-bearing rocks. J Geol Soc India 67:317–327

Mitchell RH (2010) Mineralogy of the P2-west "kimberlite", Wajrakarur, A.P, India. 6th International Dyke Conference, February 4–7, 2010, Varanasi, India. p91 (abstract)

Mitchell RH, Bergman SC (1991) Petrology of lamproites. Plenum Press, New York, **408pp**

Mitchell RH, Reed SJB (1988) Ion microprobe determination of rare earth elements in perovskites from kimberlites and alnoites. Mineral Mag 52:331–339

Moles NR (1985) Metamorphic conditions and uplift history in central Perthshire: evidence from mineral equilibria in the Foss celsian-barite-sulfide deposit, Aberfeldy. J Geol Soc Lond 142:39–52

Moro MC, Cembranos ML, Fernandez A (2001) Celsian, (Ba, K)-feldspar and cymrite from sedex barite deposits of Zamora, Spain. Can Mineral 39:1039–1051

Nayak SS, Kudari SAD (1999) Discovery of diamond-bearing kimberlite in Kalyandurg area, Anantpur district, Andhra Pradesh. Curr Sci 76: 1077–1079

Neelkantam S (2001) Exploration for diamonds in southern India. Geol Surv India Spec Publ 58:521–555

Patel SC, Ravi S, Kumar YA, Naik A, Thakur SS, Pati JK, Nayak SS (2013) Mafic xenoliths in Proterozoic kimberlites from Eastern Dharwar Craton, India: Mineralogy and P–T regime. Proceedings of the 10th International Kimberlite Conference 2:336–346

Paul DK, Nayak SS, Pant NC (2006) Indian kimberlites and related rocks: petrology and geochemistry. J Geol Soc India 67:328–355

Raith MM, Devaraju TC, Spiering B (2014) Paragenesis and chemical characteristics of the celsian−hyalophane−K-feldspar series and associated Ba-Cr micas in barite-bearing strata of the Mesoarchaean Ghattihosahalli Belt, Western Dharwar Craton, South India. Mineral Petrol 108:153–176

Rao KRP, Nayak SS, Reddy TAK, Dhakate MV, Chowdary VS, Ravi S, Suresh G, Rao KSB (2001) Geology, petrology, geochemistry, and mineral chemistry of new kimberlite finds in the Wajrakarur Kimberlite Field, Anantpur district, Andhra Pradesh. Geol Surv Ind Spl Pub 58:593–602

Ravi S, Bhaskara Rao KS, Rao KRP (1999) Search for kimberlites in the granite green stone terrain in the central segment of the Wajrakarur Kimberlite Field, Anantpur district, Andhra Pradesh. Rec Geol Surv India 132:40–43

Ravi S, Vaideswaran T, Rao KSB (2009) Field guide to Wajrakarur kimberlite field, Anantpur district, Andhra Pradesh, Geol Surv India, 43pp

Ravi S, Sufija MV, Patel SC Sheikh JM, Sridhar M, Kaminsky FV, Khachatryan GK, Nayak SS, Rao KSB (2013) Diamond potential of the Eastern Dharwar craton, Southern India, and a reconnaissance study of physical and infrared characteristics of the diamonds. Proceedings of the 10th International Kimberlite Conference 1: 335–348

Reddy TAK (1987) Kimberlite and lamproitic rocks of Wajrakarur area, Andhra Pradesh. J Geol Soc India 61:131–146

Reinecke T (1982) Cymrite and celsian in manganese-rich metamorphic rocks from Andros Island, Greece. Contrib Mineral Petrol 79:333–336

Runnells DD (1964) Cymrite in a copper deposit, Brooks Range, Alaska. Am Mineral 49:158–165

Scott Smith BH, Skinner EMW (1984) A new look at Prairie Creek, Arkansas. In: Kornprobst J (ed) Proceedings of the 3rd International Kimberlite Conference. Elsevier Press, New York 1, p 255–284

Scott Smith BH, Skinner EMW, Loney PE (1989) The Kapamba lamproites of the Luangwa valley, Eastern Zambia. In: Ross et al. (ed) q.v., 1, p 189–205

Sorokhtina NV, Chukanov NV, Voloshin AV, Pakhomovsky YA, Bogdanova AN, Moiseev MM (2008) Cymrite as an indicator of high barium activity in the formation of hydrothermal rocks related to carbonatites of the Kola Peninsula. Geol Ore Deposits 50:620–628

Stankova J, Kralik J, Schdarm B, Tomsik J, Urbanek J (1989) Cymrite from the lead-zinc deposit at Horni Benesov, northern Moravia, Czechoslovakia (in Czech with English summary). Cas Mineral Geol 34:137–150

Thy P, Stecher O, Korstgard JA (1987) Mineral chemistry and crystallization sequences in kimberlite and lamproite dikes from the Sisimut area, central west Greenland. Lithos 20:391–417

Wagner C, Velde D (1986) The mineralogy of K-richterite-bearing lamproites. Am Mineral 71:17–37